

University of Arkansas, Fayetteville

ScholarWorks@UARK

Graduate Theses and Dissertations

8-2012

Plasmonic Pervaporation via Gold Nanoparticle-Functionalized Nanocomposite Membranes

Aaron Russell

University of Arkansas, Fayetteville

Follow this and additional works at: <https://scholarworks.uark.edu/etd>



Part of the [Complex Fluids Commons](#), [Nanoscience and Nanotechnology Commons](#), and the [Thermodynamics Commons](#)

Citation

Russell, A. (2012). Plasmonic Pervaporation via Gold Nanoparticle-Functionalized Nanocomposite Membranes. *Graduate Theses and Dissertations* Retrieved from <https://scholarworks.uark.edu/etd/476>

This Dissertation is brought to you for free and open access by ScholarWorks@UARK. It has been accepted for inclusion in Graduate Theses and Dissertations by an authorized administrator of ScholarWorks@UARK. For more information, please contact scholar@uark.edu.

PLASMONIC PERVAPORATION VIA GOLD NANOPARTICLE-FUNCTIONALIZED
NANOCOMPOSITE MEMBRANES

PLASMONIC PERVAPORATION VIA GOLD NANOPARTICLE-FUNCTIONALIZED
NANOCOMPOSITE MEMBRANES

A dissertation submitted in partial fulfillment
of the requirements for the degree of
Doctor of Philosophy in Chemical Engineering

By

Aaron Gene Russell
University of Arkansas
Bachelor of Science in Chemical Engineering, 2004

August 2012
University of Arkansas

ABSTRACT

Butanol derived from biological feedstocks has significant potential as a liquid fuel source, but the separation methods used in its production can be prohibitively expensive and are therefore currently the subject of extensive research. Pervaporation is a promising membrane process that is effective in butanol separations, but involves a large energy demand. This study examines the possibility of increasing flux and energy efficiency in pervaporation via plasmonic heating of gold nanoparticle-functionalized, polymer nanocomposite membranes (AuNCMs) in lieu of conventional feed heating. An economic analysis demonstrated that plasmonic pervaporation could achieve significant reductions in energy usage and utility cost in butanol production. A novel plasmonic pervaporation system was constructed to evaluate the process experimentally. The system included uniform laser excitation and infrared thermal analysis of the membrane surface, as well as automated operation. AuNCMs, fabricated by reduction of tetrachloroauric acid by the polymer crosslinker, demonstrated stable temperature increases and flux enhancements (>100%) that increased with gold content and incident laser power.

A thermal model was developed to describe heat transfer in the system and enable calculation of membrane laser absorption efficiencies and quantification of energy loss modes. An economic investigation of the system performance was conducted by coupling the thermal model with an empirical model for flux prediction. The analysis showed that the current system performance was not sufficient to reduce the energy demand/utility cost versus conventional feed heating due to: i) heat loss to the feed and ii) low laser absorption efficiencies. The latter effect was significantly more detrimental economically and, if improved, could result in a 7-fold increase in energy efficiency.

A spectroscopic analysis method was developed to approximate AuNCM physical and optical properties to provide insights into why AuNCM absorption was low. The results indicated that only a small fraction of added Au was effectively being converted to desirable, light-absorbing nanoparticles. Evidence suggested that the remaining Au formed large, light-scattering particles, reducing the absorption efficiency of the AuNCMs. The analysis demonstrated that optimization of fabrication methods could potentially improve absorption efficiencies to near 100%, making plasmonic pervaporation economically superior to conventional methods.

This dissertation is approved for recommendation
to the Graduate Council.

Dissertation Director:

Dr. D. Keith Roper

Dissertation Committee:

Dr. Jamie Hestekin

Dr. Tom Spicer

Dr. Darin Nutter

Dr. Ingrid Fritsch

©2012 by Aaron Gene Russell
All Rights Reserved

DOCTORAL DUPLICATION RELEASE

I hereby authorize the University of Arkansas Libraries to duplicate this dissertation when needed for research and/or scholarship.

Agreed

Aaron Russell

Refused

Aaron Russell

ACKNOWLEDGEMENTS

This work would not have been possible without help from many people. I would first like to thank my advisor, Dr. D. Keith Roper, for his help and guidance throughout this process. He was always there to provide direction and assistance when I needed it, or to withhold it when he knew it would benefit me more to work it out on my own. I thank my co-advisor, Dr. Jamie Hestekin, not only for his support in my research, but also for providing me with opportunities to get involved in projects outside the lab. I also thank my committee members, Dr. Tom Spicer, Dr. Darrin Nutter, and Dr. Ingrid Fritsch, for their participation and support of my work.

I have sincerely enjoyed and benefitted in many ways from working with and learning from other graduate students – Dr. Wonmi Ahn, Phillip Blake, Gyoung Jang, Braden Harbin, Laura Velasco, Drew Dejarnette, Jeremy Dunklin, Tom Potts, and Alex Lopez. I have also been able to work with many excellent undergraduate students in the lab – Keith Berry, Matt McKnight, Adam Sharp, Jenny Pestel, Stefan Schwarz, Jacob Morgan, and many more. I learned a great deal working with them and am thankful for having the opportunity.

I thank all the faculty members and staff of the Ralph E. Martin Department of Chemical Engineering for eight wonderful years of education, as well as Dr. Greg Salamo, Dr. Morgan Ware, and Dr. Dorel Guzun of the Physics Department for their assistance and use of equipment and facilities. I am also grateful for the support of Dr. Omnia El-Hakim and the National Science Foundation Graduate Research Fellowship Program and the Walton Family Charitable Support Foundation.

Lastly, I would like to thank my parents, Jeff and Sharon, and my brother and sister, Josh and Chelsea, for everything they have done and continue to do to support me.

DEDICATION

I dedicate this dissertation to my incredible wife, Jamie. Over the past four years, she has been an unfailing source of encouragement and support. I would not be where I am without her.

TABLE OF CONTENTS

CHAPTER 1.....	1
1.1 MOTIVATION OF THE PRESENT WORK	1
1.2 PLASMONIC HEATING IN GOLD NANOPARTICLES	3
1.3 HYPOTHESIS.....	4
1.4 POTENTIAL FOR ECONOMIC IMPACT	4
1.5 SIGNIFICANT ADVANCES OF THE PRESENT WORK	5
CHAPTER 2.....	9
2.1 SIGNIFICANCE OF THE PRESENT WORK	9
2.2 PLASMONIC PERVAPORATION SYSTEM	11
2.2.1 LASER PERVAPORATION CELL AND EXPERIMENTAL SETUP.....	11
2.2.2 AUTOMATED OPERATION AND DATA CAPTURE.....	12
2.2.3 GOLD-PDMS MEMBRANES	13
2.3 PERVAPORATION PERFORMANCE	15
2.3.1 THERMAL BEHAVIOR IN OPERATION	15
2.3.2 FLUX ENHANCEMENT	18
2.3.3 SOLUTION DIFFUSION MODEL	20
2.3.4 AuNCM PERMEANCE.....	23
2.4 CONCLUSIONS.....	24
CHAPTER 3.....	35
3.1 SIGNIFICANCE OF THE PRESENT WORK	35
3.2 THERMOPLASMONIC MODELING	36
3.2.1 CAPILLARY THERMAL MODEL	36
3.2.2 PLASMONIC PERVAPORATION MODEL	39
3.2.3 ACCURACY OF INFINITE FIN APPROACH.....	41
3.2.4 MODEL RESULTS	42
3.3 PERVAPORATION MODELING	47
3.3.1 ACTIVATION ENERGY ANALYSIS	48

3.3.2	PERSPECTIVES ON AuNCM PERMEANCE.....	49
3.3.3	FLUX PREDICTION.....	51
3.4	COUPLED MODEL FOR ECONOMIC ANALYSIS.....	52
3.5	CONCLUSIONS.....	54
CHAPTER 4.....		63
4.1	SIGNIFICANCE OF THE PRESENT WORK	63
4.2	UV-VIS SPECTROSCOPIC ANALYSIS	65
4.2.1	SPECTRAL ADJUSTMENT	66
4.2.2	SPECTRAL RESULTS.....	67
4.3	ESTIMATION OF AuNP CONCENTRATION	69
4.3.1	INSIGHTS INTO AuNP GROWTH	71
4.3.2	GOLD UTILIZATION	72
4.4	EVIDENCE OF THE PRESENCE OF LARGE PARTICLES.....	73
4.5	CONCLUSIONS.....	76
CHAPTER 5.....		83
5.1	SUMMARY OF FINDINGS	83
5.1.1	PLASMONIC PERVAPORATION SYSTEM AND PERFORMANCE	83
5.1.2	THERMAL MODELING	84
5.1.3	PERVAPORATION MODELING AND ECONOMIC ANALYSIS.....	85
5.1.4	AuNCM CHARACTERIZATION	85
5.2	ONGOING AND FUTURE WORK.....	86
5.2.1	IMPROVEMENTS IN CURRENT SYSTEM	86
5.2.2	INVESTIGATION OF SELECTIVITY	86
5.2.3	AuNCM THERMAL PROPERTIES	87
5.2.4	MEMBRANE OPTIMIZATION AND CHARACTERIZATION	87
5.2.5	ADDITIONAL APPLICATIONS.....	88

LIST OF FIGURES

Figure 1.1. Illustration of thermoplasmonic heating in AuNPs on silica substrates.	7
Figure 1.2. Reduction in energy usage and utility costs as a function of light source efficiency in plasmonic pervaporation.	8
Figure 2.1. Schematic of the experimental plasmonic pervaporation system and the laser excited pervaporation cell. Image shows plasmonic pervaporation cell during operation.....	26
Figure 2.2. Values of laser power extinction fraction (532 nm) for AuNCMs from three different batches at four different values of gold content. Each AuNCM is pictured in the inset. Extinction fractions of the glass substrate and bare PDMS were measured independently and have been factored out of the values in the figure – therefore a 0.0% Au membrane has an extinction fraction of zero on this scale.	27
Figure 2.3. Box and whisker plots of membrane thermal distributions during the 5-10 h period of pervaporation experiments for the four membranes (0.0, 0.1, 0.4, and 0.6% Au) at four levels of laser irradiation (left to right, 0, 250, 500, and 750 mW). The mean temperature for each point is also shown (red diamonds). Inset shows a representative spatial thermal distribution across the membrane.	28
Figure 2.4. Average membrane surface temperature with time for the 0.0, 0.1, 0.4, and 0.6% Au membranes irradiated with 0, 250, 500, and 750 mW laser power during butanol pervaporation experiments. Regions (a), (b), and (c) in the 0.6% graph indicate dynamic thermal regions that are illustrated in Figure 2.5.	29
Figure 2.5. Average temperature of a 0.6% AuNCM with time during the three dynamic thermal regions of the plasmonic pervaporation experiments (750 mW laser irradiation): (a) when the pump is turned on (diamonds), (b) when the laser is turned on and the thermal mass of the membrane dominates (squares), and (c) region after turning on the laser in which the thermal mass of butanol and the cell wall dominate (triangles). Regions (a), (b), and (c) correspond to those indicated in Figure 2.4.	30
Figure 2.6. The average steady state temperature change during butanol pervaporation for membranes of different Au content as a function of incident laser power. Error bars show one standard deviation of 300 measurements taken over the period of 5 h.	31
Figure 2.7. Flux of butanol as a function of time for the four membranes with varying incident laser powers. The data points have been smoothed (boxcar 3) and shifted in time such that the laser is turned on at t=2 h. A dynamic region (shaded) follows t=2 h during which steady state is reached.	32
Figure 2.8. (a) Flux of butanol as a function of incident laser power. Error bars represent one standard deviation of 15 flux readings taken over a 5 h period. (b) The fractional increase in flux as a function of incident laser power. Lines in (b) represent least squares regressions of the data.	33

Figure 2.9. Fractional change in permeance as a function of membrane temperature change for the four membranes studied. Lines represent linear regressions of each data set.....	34
Figure 3.1. Diagram of heat transfer in an open, silica capillary plated with AuNPs.....	55
Figure 3.2. Schematic of heat transfer from the laser heated AuNCM in the plasmonic pervaporation system.	56
Figure 3.3. Comparison of feed cell temperatures measured experimentally and calculated using infinite fin model for each membrane at 250, 500, and 750 mW laser irradiation (left to right). 57	
Figure 3.4. Membrane assembly (membrane and stainless steel mesh) laser absorbance fractions for the four membranes at three levels of incident laser power. Representation of the cumulative uncertainty inherent to these values is not shown here, but is discussed at length in Chapter 3. . 58	
Figure 3.5. Energy consumed by vaporization of butanol permeate on two different bases: i) as a percentage of the incident light and ii) as a percentage of the absorbed light (incident light multiplied by the absorbance fractions in Figure 3.4) at 250, 500, and 750 mW laser irradiation (left to right).	59
Figure 3.6. Comparison of experimentally measured fluxes and simulated fluxes generated by an empirical model for membrane permeance based on Au content.	60
Figure 3.7. Realization (shaded regions) of predicted reduction in energy demand (blue) and utility cost (red) from experimental plasmonic pervaporation results and modeling. Lines show original ideal case (Figure 1.2), shaded regions outline predicted realization according to Au content (top = 0.6% Au, bottom = 0.0% Au) based on (a) absorbed light and (b) incident light. 61	
Figure 4.1. Unadjusted (a) and laser extinction adjusted (b) UV-vis spectra of 12 AuNCMs (three batches at the 4 concentrations shown). Solid, dashed, and dotted lines indicate batch 1, 2, and 3, respectively.	77
Figure 4.2. Localized surface plasmon wavelength (a) and average AuNP diameter (b) for the 12 AuNCMs (three batches at the 4 concentrations shown).	78
Figure 4.3. Values of estimated laser power consumption (excludes scattered laser light) fraction for Au-NCMs from three different batches at four different values of gold content.	79
Figure 4.4. Estimated concentration of AuNPs (a) of the average diameters given in Figure 4.2 and percent conversion of added Au to AuNPs of this type (b).	80
Figure 4.5. Increasing opacity of AuNCMs with increasing Au content indicating increasing concentration of large particles.	81
Figure 4.6. Simulations of transmittance fraction of 532 nm light due to particle scattering for four concentrations of AuNCM for particle diameters from 0-700 nm and for 0-100% conversion of total Au content to particles of that size.	82

LIST OF TABLES

Table 3.1. Thermoplasmonic model results for each pervaporation data set. All values are in units of mW..... 62

LIST OF NOMENCLATURE

ABBREVIATIONS

Au	A_E
AuNCM	Gold
AuNP	Gold nanoparticle-functionalized nanocomposite membrane
CA	Gold nanoparticle
IR	Cellulose acetate
LSPR	Infrared
NP	Localized surface plasmon resonance
PDMS	Nanoparticle
PI	Polydimethylsiloxane
SD	Polyimide
SS	Solution diffusion
SS ΔT	Steady state
TCA	Steady state temperature change
TEM	Tetrachloroauric acid

SYMBOLS

a	
A_1	Conversion factor from liquid level change to volume change [pixels mL ⁻¹]
A_2	Empirical fitting constant for permeation activation energy [J g ⁻¹]
A_{506}	Empirical fitting constant for permeation activation energy [J g ⁻¹]

Spectral extinction at 506 nm	$C_{p,j}$ D
Area for D_i	
evaporation in the capillary system	E_p h_{conv}
$[m^2]$	h_{fin}
A_c	Area for conduction heat transfer $[m^2]$
A_{fin}	Fin cross-sectional area $[m^2]$
a_p	Empirical fitting constant for the molar extinction coefficient
A_s	Area for convention and radiation heat transfer in capillary system $[m^2]$
$Au\%$	Gold mass percent in membrane [%]
A_λ	Spectral extinction at wavelength, λ
B_1	Empirical constant for permeation activation energy $[mol\ cm^{-2}\ s^{-1}\ torr^{-1}]$
B_2	Empirical fitting constant for permeation activation energy
$C_\%$	Percentage of Au converted to 532 nm-absorbing particles [%]
C_{abs}	Absorbance cross-section $[m^{-2}]$
C_{AuNP}	Membrane nanoparticle concentration $[NP\ mL^{-1}]$
C_{ext}	Extinction cross-section $[m^{-2}]$
c_i	Molar concentration of i $[mol\ m^{-3}]$
$c_{i,0}$	Molar concentration of i in the feed $[mol\ cm^{-3}]$
$c_{i,0,(m)}$	Molar concentration of i in the membrane on the feed side $[mol\ m^{-3}]$
$c_{i,\ell(m)}$	Molar concentration of i in the membrane on the permeate side $[mol\ m^{-3}]$
$C_{p,f}$	Heat capacity of the fluid $[J\ g^{-1}\ K^{-1}]$

Heat capacity of i

$[\text{J g}^{-1} \text{K}^{-1}]$

Particle diameter

$[\text{nm}]$

Diffusivity of i

$[\text{cm}^2 \text{s}^{-1}]$

Activation energy

of permeation $[\text{J g}^{-1}]$

Convection heat

transfer coefficient

$[\text{W m}^{-2} \text{K}^{-1}]$

Convection heat

transfer coefficient

for an infinite fin

$[\text{W m}^{-2} \text{K}^{-1}]$

H_i	Henry's law constant for i [torr cm ⁻³ mol ⁻¹]
i	Arbitrary component designation
I	Incident laser power [W]
I_T	Transmitted laser power [W]
j	Mass flux of butanol [kg m ⁻² h ⁻¹]
J_i	Molar flux of i [mol cm ⁻² s ⁻¹]
k	Thermal conductivity of capillary system mount [W m ⁻¹ K ⁻¹]
k_c	Capillary system mass transfer coefficient [cm ² s ⁻¹]
k_{fin}	Thermal conductivity of an infinite fin [W m ⁻¹ K ⁻¹]
K_i^G	Gas phase sorption coefficient of i [mol cm ⁻³ torr ⁻¹]
$K_{i,0}^G$	Pre-exponential factor for the gas phase sorption coeff. of i [mol cm ⁻³ torr ⁻¹]
K_i^L	Liquid phase sorption coefficient of i
k_p	Empirical fitting constant for the molar extinction coefficient
ℓ	Membrane thickness [m]
L	Conduction length in capillary system [cm]
\dot{m}	Mass transfer rate [g s ⁻¹]
m_{Au}	Mass of gold added to membrane solution [g]
m_f	Mass of fluid added to capillary [g]
m_j	Mass of system component j
MW_{Au}	Molecular weight of gold [g mol ⁻¹]
MW_f	Fluid molecular weight [g mol ⁻¹]
MW_i	Molecular weight of i [g mol ⁻¹]
$T(x)$	Temperature as a function of location on an infinite fin [°C]

N_A	Avogadro's constant [atoms mol ⁻¹]
N_{Au}	Number of gold atoms in a gold nanoparticle [atoms NP ⁻¹]
n_m	Refractive index of the polymer matrix
p	Perimeter of an infinite fin [m]
P_1	Total pressure on the feed side [torr]
P_2	Total pressure on the permeate side [torr]
P_i^G	Gas phase permeability coefficient [mol m ⁻¹ s ⁻¹ torr ⁻¹]
$p_{i,0}$	Vapor pressure of i on the feed side [torr]
$p_{i,\ell}$	Vapor pressure of i on the permeate side [torr]
\overline{P}_i	Permeance of i [mol m ⁻² s ⁻¹ torr ⁻¹]
$\overline{P}_{i,0}$	Pre-exponential factor for permeance of i [mol m ⁻² s ⁻¹ torr ⁻¹]
Q_{abs}	Incident laser power absorbed (consumed) [W]
Q_{cond}	Power loss by conduction [W]
Q_{conv}	Power loss by convection [W]
q_{exp}	Heat of isothermal expansion [J g ⁻¹]
Q_{ext}	Incident laser power extinguished [W]
Q_{fin}	Power loss from an infinite fin [W]
Q_I	Power input from laser [W]
$Q_{O,i}$	Power loss from mode i [W]
Q_{rad}	Power loss by radiation [W]
R	Gas constant [J g ⁻¹ K ⁻¹]
T	Temperature [°C]
T_{amb}	Temperature of ambient environment [°C]

T_b	Base temperature of an infinite fin [°C]
V	Volume of membrane solution [mL]
x	Distance along an infinite fin [m]
n_p	Refractive index of particles
r	Particle radius [nm]

GREEK LETTERS

ΔC_f	Concentration difference [mol cm ⁻³]
ΔH_s	Heat of solution [J g ⁻¹]
ΔH_{vf}	Heat of vaporization [J g ⁻¹]
Δp	Change in liquid level [pixels]
Δt	Time between experimental readings [min]
ε	Emissivity
ε_λ	Molar extinction coefficient [L m ⁻¹ mol ⁻¹]
η_T	Nanoparticle transduction efficiency
λ	Wavelength [nm]
ρ	Density of butanol [kg m ⁻³]
σ	Stefan-Boltzmann constant [W m ⁻² K ⁻⁴]
Φ_p	Particle volume fraction

CHAPTER 1

INTRODUCTION TO PLASMONIC PERVAPORATION

1.1 MOTIVATION OF THE PRESENT WORK

Reduction of society's dependence on fossil fuels remains one of the most pressing issues facing scientists and engineers today. Considerable research is being done to increase the viability of alternative energy sources such as wind, solar, and biofuels. In recent years, butanol derived from biological sources, including bacterial fermentation of cellulosic feedstocks and algae, has become increasingly popular as a potential liquid fuel source. Butanol boasts many significant advantages relative to other biofuels. Most notably, butanol has the ability to be used directly in unmodified gasoline engines, either pure or blended with gasoline in any concentration, and it is not highly corrosive and can therefore be transported using the current infrastructure. Additionally, it has a higher energy density and lower vapor pressure than ethanol – the most widely used biofuel.^{1, 2} These benefits make butanol highly attractive as part of the eventual solution to society's energy needs.

Since butanol is produced in a dilute aqueous solution, separation comprises a large part of the production costs. In general, the economy of scale for chemical production favors large, centralized operations, but for some biofuel feedstocks like those used for butanol production, the cost of material transport can dominate and shift the economic balance toward smaller, localized facilities. At these small scales, the economic feasibility of conventional distillation

falls and alternative separation techniques become more advantageous.³ Additionally, since butanol is produced in dilute solution, distillation is a particularly energy-intensive since butanol has a higher boiling point than water. Researchers have projected that a pure distillation approach to separating butanol from a conventional fermentation broth has an energy demand of 50%⁴ to >100%⁵ of the energy content of butanol. An internal economic analysis performed by Dr. Jamie Hestekin's research group demonstrated the utility cost associated with this distillation can account for as much as 75% of the total operating cost of production. Thus, efficient alternative butanol separation methods must be employed to make it economically competitive with fossil fuels. One method that has recently garnered considerable attention is pervaporation.

Pervaporation is a membrane process that utilizes differences in vapor pressure as a driving force for separation. Components are vaporized across the membrane at different rates according to both their respective vapor pressures and their permeability in the membrane. Pervaporation is an effective and environmentally friendly⁶ means of overcoming azeotropes and separating dilute solutions. For these reasons, butanol has found wide-ranging applications in petroleum refining,⁷⁻⁹ organic-organic separations,^{10, 11} alcohol dehydration,^{12, 13} and the removal of dilute organics from aqueous solutions such as those resulting from the production of biofuels.¹⁴⁻²⁰ It is utilized both as a stand-alone process and also in hybrid distillation-pervaporation processes as a finishing step to reduce energy demand.^{13, 21} Even though pervaporation is currently the subject of extensive research efforts, there is still significant room for technological improvement.^{3, 22}

The energy requirements of pervaporation can be substantial since the process is run at elevated temperatures, the desired component is typically dilute, and the permeate must be vaporized for the separation to occur. This vaporization induces two effects that reduce the

efficiency of the process: i) a thermal gradient from the feed to the permeate side of the membrane which reduces mass transfer²³⁻²⁵ and ii) feed cooling which results in the need for additional heating between membrane stages.²⁶ The latter effect significantly increases the process cost and is the subject of many investigations on reducing the energy demand of the process. Other significant issues with current pervaporation technology include low production rate (flux) and loss of efficiency due to concentration polarization in the separation of dilute organics from aqueous solutions.²² This study examines a possible means of addressing each of these issues by delivering energy to the membrane itself.

1.2 PLASMONIC HEATING IN GOLD NANOPARTICLES

Gold nanoparticles (AuNP) have generated wide interest due to their ability to undergo thermoplasmonic heating induced by electromagnetic energy. Thermoplasmonic heating occurs when incident light at resonant frequencies is absorbed by the NP causing collective oscillations of conduction electrons on the NP surface. This resonant electron oscillation is known as localized surface plasmon resonance (LSPR)²⁷ and as it decays, the excited electrons couple with phonons (i.e. crystal lattice vibrations) in the NP causing an increase in thermal energy which is then transferred to the NP environment by phonon-phonon coupling (see Figure 1.1).²⁸⁻³⁰ This effect has been exploited in biomedical therapeutics including non-invasive photothermal tumor cell ablation³¹⁻³³ or targeted release of encapsulated materials,³⁴ local protein or RNA unfolding,³⁵ nanoscale substrate modification,³⁶ nanomaterials modification,³⁷⁻³⁹ and improved performance of catalytic systems.⁴⁰⁻⁴²

NP composition, size, morphology, and dielectric environment all affect the fraction of incident light that is transmitted, scattered, or absorbed. The fraction of extinguished light (scattered plus absorbed light) that is absorbed and converted to heat is defined as the

transduction efficiency.⁴³ For AuNPs under certain conditions (size, refractive index, etc.), the transduction efficiency approaches 100% meaning that virtually all extinguished light is absorbed and converted to heat.⁴³⁻⁴⁵ Thus, AuNPs are highly efficient at capturing light and, with their incorporation in certain systems, can be used to efficiently transduce light to thermal energy in a target region while the remaining elements of the system are relatively unaffected.⁴²

1.3 HYPOTHESIS

The hypothesis guiding this work was that the targeted input of energy via plasmonic heating of AuNP-functionalized, polymer nanocomposite membranes (AuNCM) will increase flux and energy efficiency in the pervaporation of butanol. Direct heating of the membrane in this manner would eliminate the need to heat the entire feedstock as well as the need to reheat the retentate between membrane stages since the heat of vaporization for the permeate would be provided in the membrane. In practice, this could be achieved by highly efficient LED excitation of the AuNP by an optical fiber/diffuser within the membrane module. This process would benefit both a purely pervaporative separation as well as the integrated pervaporation-distillation approaches discussed above wherein necessary heat makeup between pervaporation modules causes both significant operating and capital costs.¹³

1.4 POTENTIAL FOR ECONOMIC IMPACT

Two competing factors will determine the cost savings of the proposed process: 1) the reduction in capital and utility costs due to increased flux and decreased energy demand and 2) the increased costs associated with adding gold (Au) to the membrane and using electrical (LED) heating as opposed to steam. An initial analysis of energy demand and utility cost reduction was performed to estimate the savings that could be achieved from plasmonic pervaporation. The analysis used a basis of a butanol fermentation from which butanol would be removed

continuously by pervaporation before recycle of the broth to the fermenter. The energy requirements include: 1) latent heat needed to vaporize permeate, 2) energy needed to heat material to the pervaporation utility temperature, and 3) energy to cool retentate for recycle to the fermenter. Pervaporation occurs at a selectivity of 45 and total flux of $518 \text{ g/m}^2 \text{ h}$ at 70°C .¹⁹ Energy is consumed in the system by steam heating the broth from the fermentation operating temperature of 37°C to 70°C to feed the pervaporation system at a feed rate of 1440 mL/min and cooling of retentate with cooling water from 70°C to 37°C (minus the energy lost from evaporation) to recycle to the fermentor.^{26, 46} Plasmonic heating of the membrane was assumed to eliminate the need for steam heating and water cooling. This would occur as an increase of membrane temperature from laser irradiation to achieve an equivalent flux, but with no loss of energy by any mechanism other than vaporization.

The result is a *reduction in energy use and utility cost by factors up to 12.2- and 5.7-fold*, respectively (see Figure 1.2). These reduction factors increase in proportion to the efficiency of converting electricity to monochromatic light. This scenario assumes an ideal system in which there is 100% absorption of incident light and no loss of heat to the feed. It is provided as the limiting case for the system described above. The utility cost reduction factor at a large scale is less than the energy reduction factor because cooling water and steam are cheaper at a large scale than electricity. Consideration of the capacity for reduction of energy demand and utility cost combined with the fact that energy cost accounts for a large percentage of the production cost of biobutanol provides a strong basis of support for the potential cost savings of plasmonic pervaporation.

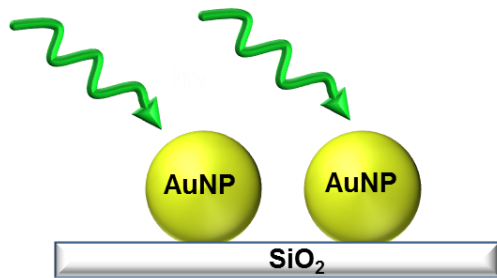
1.5 SIGNIFICANT ADVANCES OF THE PRESENT WORK

A considerable amount of research and development is required to make plasmonic pervaporation a viable process. The significant advances made in this study are listed below:

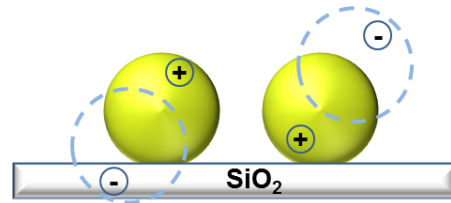
1. A plasmonic pervaporation system was developed that enabled uniform laser excitation of the membrane, thermal analysis of the entire membrane surface, and automated operation and data capture.
2. AuNCMs were fabricated in varying concentration and utilized in the plasmonic pervaporation system, demonstrating flux enhancements up to 117% that increased according to Au content and incident laser power.
3. The thermal behavior of the AuNCMs in operation was described using a continuum heat transfer model to quantify the modes of energy loss from the system and the AuNCM absorption efficiencies.
4. The heat transfer model was coupled with an empirical relation to predict flux based on Au content and incident laser power to estimate realization of the economic impact predicted above.
5. A method was developed to estimate AuNCM properties (concentration, gold utilization, etc.) based on laser extinction, spectral analysis, Beer-Lambert's law, and Mie theory.

Each of these advances will be discussed in detail in the following chapters. The final chapter will summarize the findings of this study and suggest areas of focus for future work.

1) Gold nanoparticle (AuNP) irradiated with resonant light



2) Localized surface plasmon (LSP) is created



3) LSP decays to thermal energy that is transferred to the environment

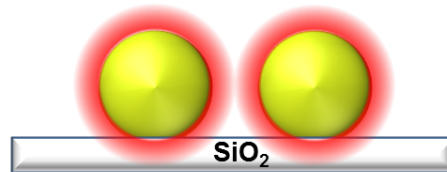


Figure 1.1. Illustration of thermoplasmonic heating in AuNPs on silica substrates.

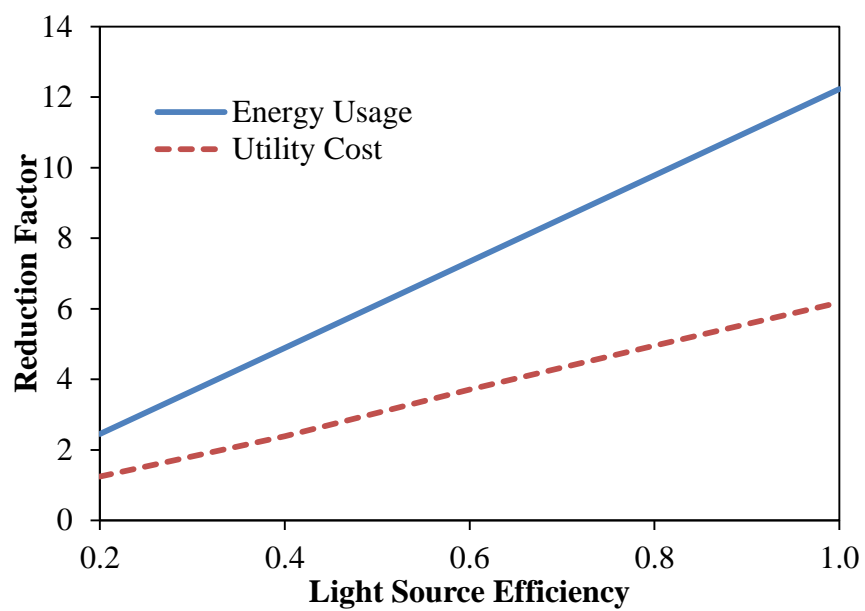


Figure 1.2. Reduction in energy usage and utility costs as a function of light source efficiency in plasmonic pervaporation.

CHAPTER 2

PLASMONIC PERVAPORATION

2.1 SIGNIFICANCE OF THE PRESENT WORK

This chapter details the design, operation, and performance of the plasmonic pervaporation system. The purpose of plasmonic pervaporation is to reduce the energy demand of pervaporation by direct heating of the AuNP-functionalized membrane to provide the requisite heat of vaporization to the permeate and eliminate the need to heat the entire feedstock. High flux is maintained by increasing the temperature of the membrane itself. The majority of the current research in pervaporation energy demand reduction is focused on preventing or recapturing heat lost due to vaporization of the permeate. This is typically facilitated by complicated membrane module designs that heat the feed while it is in the module. Some approaches have focused on capturing energy from the distillate vapor stream – in a hybrid distillation-pervaporation system – by funneling it through a “heat integrated” pervaporation module.^{47, 48} A commercially available shell and tube type pervaporation membrane module offered by Sultzer Chemtech enables isothermal operation by thermal fluid heating (steam or oil) of the feed within the module itself.¹³ Another method, termed “thermo pervap,” attempts to recapture the heat of vaporization by condensation of the permeate from thermal contact with incoming feed at a lower temperature. The feed still requires additional heating before exposure to the membrane.⁴⁹ While these approaches have demonstrated success in reducing energy

demand, they only serve to prevent or recapture feed thermal losses and are not designed to increase flux, reduce base thermal energy demand, or break the thermal gradient that develops across the membrane reducing mass transfer efficiency.^{23, 24} Plasmonic pervaporation addresses each of these limitations.

Microwave heating has been shown to increase CO₂ permeabilities and diffusion coefficients when applied to a membrane system,⁵⁰⁻⁵² but it has limited viability for the current application due to its tendency to heat water (and butanol to a lesser extent) combined with its inability to target the membrane. Additionally, direct local heating of membranes using resistive electrical heating has previously been studied to reduce energy demand and improve flux and selectivity in membrane separations. Boddeker *et al.* demonstrated that both flux and selectivity could be increased in the pervaporation of high-boiling compounds by using a conductive steel mesh as both an internal membrane support and resistive heater. The moderate improvements were attributed to a reversal of the thermal gradient between the feed and permeate sides of the membrane.²⁵ In a similar system, resistive heating of a silicone rubber coated aluminum membrane was used to allow isothermal operation in crossflow, ethanol/water pervaporation modules at low flowrates.⁵³ However, these methods result in sacrificing a substantial amount of expensive membrane area by incorporation of the large scale metal structures, potential contact issues between the metal and polymer, and nonuniform membrane heating. These issues can all be overcome by using nanoscale media excited by electromagnetic fields.

The use of AuNPs in filtration to increase flux is not without precedent. Vanherck *et al.* have recently (2011) begun investigating the flux and selectivity effects of incorporating laser heated AuNPs in cellulose acetate (CA) and polyimide (PI) nanofiltration membranes. It was demonstrated that this technique increased the single component flux of ethanol substantially

more than that of water under the same conditions in CA membranes – which the authors concluded demonstrates an increase in flux without a reduction in selectivity – and that flux could be increased without affecting solute rejection in dense PI membranes.^{54, 55} However, the work performed and the conclusions made had several limitations: thermal analysis of the membrane in operation was not possible, measured fluxes were of single components and the lack of reduced selectivity was attributed to heat transfer effects that would not be present in mixtures, porous (pressure driven) rather than dense membranes were used and thus the driving force is not affected, quantitative modeling of the effects was not performed, conclusions regarding the energy demand were not fully explored, and a beneficial application was not identified. The plasmonic pervaporation system enables each of these limitations to be addressed and utilizes plasmonic heating where there is large economic advantage in terms of energy demand.

2.2 PLASMONIC PERVAPORATION SYSTEM

2.2.1 Laser Pervaporation Cell and Experimental Setup

The entire experimental plasmonic pervaporation system setup, a detailed schematic of the laser pervaporation cell, and an image of the cell in operation are shown in Figure 2.1. The custom laser pervaporation cell forms the heart of the plasmonic pervaporation system. The cell is comprised of two custom glass tubes (feed and permeate) and the membrane assembly. The feed tube is fitted with a quartz window opposite the membrane for laser introduction and two graduated pipettes that function as level indicators and enable continuous flux measurement. A thermocouple was affixed to the outside of the feed tube 1.7 cm away from the membrane to record the feed temperature at that point. The permeate tube is fitted with a vacuum port and a germanium window located opposite the membrane. The germanium window is highly

transparent to infrared (IR) radiation and allows the temperature of the entire membrane surface (7178 individual points) to be evaluated using an IR camera (ICI 7320 P-Series, Infrared Cameras Inc., Beaumont, TX). The active membrane area is circular with a 15 mm diameter giving an area for each thermal node of $\sim 2.5 \times 10^{-2} \text{ mm}^2$. Sandwiched between the permeate and feed tubes is the membrane assembly which includes two polydimethylsiloxane (PDMS) gaskets, the AuNCM, and a stainless steel mesh that provides mechanical support as well as additional laser absorption. The membrane assembly is held between the feed and permeate tubes by an aluminum clamp/stand (seen in the image). A continuous wave, 532 nm diode laser (MXL-H-532, CNI, Changchun, China) was used to heat the membrane. A power meter (PM310D, Thorlabs, Newton, NJ) was used to measure incident laser power before and after each run to ensure consistency.

The laser pervaporation cell was enclosed in a plexiglass box to minimize convection currents. A small amount of air was continually drawn through the box to prevent butanol buildup in the ambient environment. A vacuum pump (DV-4E, JB Industries Inc., Aurora, IL) was used to evacuate the permeate side and permeate was condensed and captured using a cold trap (dry ice and isopropyl alcohol). Permeate pressure was controlled using a vacuum regulator (EW-07061-30, Cole-Parmer, Vernon Hills, IL) and continuous measurements were taken using an absolute capacitance manometer (722B-100, MKS Instruments, Andover, MA), a data acquisition card, and LabVIEW Signal Express (National Instruments, Austin, TX).

2.2.2 Automated Operation and Data Capture

The system was designed to enable automated operation and data collection. Permeate pressure and membrane thermal images were recorded continuously using data acquisition software. Permeate pressure was set and maintained between 1.8 and 2.2 torr for all experiments

using the vacuum regulator. Feed level changes, as well as ambient condition readings (temperature and humidity) and the feed temperature, were collected by taking intermittent images (every 20 min) using a webcam and image acquisition software. Small styrofoam balls were placed in the graduated level indicators to increase visibility of the liquid level. The images were analyzed with a Matlab script to calculate flux rates using a measured conversion factor of 281.33 pixels/mL volume change. This equates to a level of discretization of $4.89 \times 10^{-2} \text{ kg m}^{-2} \text{ h}^{-1}$ for 20-min readings; however, Matlab enabled evaluation of partial image pixels (<0.1 pixel) and therefore the maximum level of discretization was significantly higher. The flux was calculated as

$$j = \frac{a\rho\Delta p}{A_m\Delta t} \quad (2.1)$$

where j is the pure butanol mass flux, ρ is the density of butanol, a is the conversion factor from change in liquid level position to volume change, Δp is the change of liquid level position in the level indicator (in pixels), A_m is the active membrane area, and Δt is the time period over which the liquid level change occurred (20 min).

2.2.3 Gold-PDMS Membranes

In order to achieve the most efficient use of incident light within the plasmonic pervaporation system and realize the maximum economic impact, the nanocomposite membranes utilized in the pervaporation system must: 1) be highly concentrated with AuNPs that absorb at the excitation wavelength, 2) utilize facile, reproducible fabrication methods, and 3) be as cost-effective as possible. A brief description of the AuNCMs used in this work is provided here, and a full characterization with regard to these criteria is the subject of Chapter 4.

Briefly, the AuNCMs were fabricated by mixing tetrachloroauric acid (TCA) in varying concentrations in uncured PDMS to promote Au reduction to AuNPs facilitated by the silicon-hydride active sites in the PDMS crosslinker.⁵⁶ The solution was then spincoated on a glass slide and cured at 150 °C to form dense AuNCMs with thicknesses between 74 and 79 microns. Detailed fabrication methods and operational parameters are included in a manuscript currently in preparation to be submitted for publication.⁵⁷ The AuNCMs were prepared in four concentrations (0.1, 0.4, 0.6, and 0.75% Au by mass) and three batches were made at each concentration. The resulting laser extinction capability, measured using the power meter as incident power minus transmitted power, of each AuNCM from each batch is shown in Figure 2.2. The extinction measurements were taken with the AuNCMs attached to glass substrates, but the extinction fractions of the glass (0.08) and bare PDMS (0.07) were measured independently and have been factored out of the values in the figure – therefore, on this scale, a 0.0% Au membrane would have an extinction fraction of zero. Images of the AuNCMs are shown in the Figure 2.2 inset. Laser extinction increased logarithmically as a function of total Au content in the AuNCM. Of particular note is the low variance in the relative extinction between batches at the same concentration. The standard deviations of the extinction fraction values across batches are 0.013, 0.021, 0.015, and 0.010 for 0.1, 0.4, 0.6, and 0.75% Au, corresponding to only 8.95, 4.72, 2.67, and 1.54% of the mean extinction fraction values, respectively. Thus, it is evident that highly consistent laser extinction fraction values can be obtained by this method. This result is compelling given the ease and rapidity of the fabrication technique, and it supports the conclusion that even higher levels of reproducibility could be achieved with further optimization.

Pervaporation experiments were performed with one AuNCM from each of the three lower concentrations and one bare PDMS membrane (0.0, 0.1, 0.4, and 0.6%). The 0.75%

AuNCM did not fully cure, most likely due to overconsumption of crosslinker by the reduction of Au, and was not suitable for use in the plasmonic pervaporation system. Each membrane was tested at four levels of incident laser power: 0, 250, 500, and 750 mW for >10 h to ensure steady state (SS) operation was reached. All analysis of SS operation data discussed below was taken from the time period spanning 5-10 hours following pump startup.

2.3 PERVAPORATION PERFORMANCE

2.3.1 Thermal Behavior in Operation

Laser irradiation of the AuNCMs during operation of the plasmonic pervaporation system resulted in stable increases in membrane temperature that rose according to membrane Au content and incident laser power. The laser spot was expanded to irradiate the entire surface of the membranes; however, the membranes developed a nonuniform thermal profile during operation. The profile likely developed due to an uneven power distribution in the laser spot and radial heat transfer from the membrane. To illustrate the variation in the thermal profile, Figure 2.3 shows box and whisker plots of membrane spatial thermal distributions averaged over the 5-10 h period of the pervaporation experiments for the four membranes (0.0, 0.1, 0.4, and 0.6% Au) at all four levels of laser irradiation (left to right, 0, 250, 500, and 750 mW). The average (mean) temperature for each point is also shown (red diamonds). The inset in Figure 2.3 shows a representative spatial thermal distribution across the membrane. The membrane thermal profile appears parabolic with the highest temperatures concentrated slightly removed from the center (likely due to power distribution in the laser spot). The maximum temperature spread across the membrane grows with increasing laser power for all membranes, as does the difference between the 1st and 3rd quartiles. Although the thermal distribution widens with laser power, the mean and median of each data set remain very closely aligned. This alignment indicates that the

spatial temperature profile of the membrane follows a normal distribution and the average temperature of each set can be treated as a representative value. Thus, the average temperature will be used in all further discussion and modeling of the membrane thermal response.

It is important to note that there is a significant increase in temperature observed when the bare PDMS membrane is used. As PDMS is highly transparent to visible light, the majority of incident laser light absorption and conversion to heat within the membrane assembly is facilitated by the stainless steel mesh. Stainless steel can function as an efficient absorber of visible laser light, achieving absorbance as high as 40-65% at 527 nm depending on the type of steel and the surface roughness.⁵⁸ The total percentage of incident laser light extinguished by the bare stainless steel membrane and mesh (measured with the power meter) was $(51.2 \pm 0.8)\%$. The standard deviation of 0.8% represents variation across three laser powers: 100, 500, and 1000 mW. The cross-sectional area of the mesh in the laser path was estimated to be $7.41 \times 10^{-5} \text{ m}^2$, based on measurements with a micrometer, or 41.9% of the total membrane area. The remaining fraction of extinguished light (of the 51.2%) may be lost due to scattering by the PDMS.

Figure 2.4 shows the average membrane surface temperature with time for each membrane at 0, 250, 500, and 750 mW of laser irradiation during the entire 10 h butanol pervaporation experiments. The data has been shifted slightly in time to align the point at which the laser is turned on for each run (2 h). At least 2 h of data is captured before turning on the laser to ensure SS behavior is reached and an accurate SS temperature change (SS ΔT) can be measured. As the figure demonstrates, the thermal behavior of the membranes in the SS regions is highly stable throughout the course of the pervaporation runs, with and without laser irradiation. The output power of the laser can vary with time and there is no way to measure this

occurrence throughout the experiments. However, the stability of the data sets suggests that no significant variation in laser power occurred. Average SS ΔT s and flux values reported below were calculated from the 5-10 h region of each run.

The regions indicated by (a), (b), and (c) in the 0.6% graph in Figure 2.4 represent the three dynamic thermal regions that occur in the data sets. These dynamic regions are shown in detail for the 0.6% AuNCM at 750 mW laser power in Figure 2.5. There is an initial drop in temperature of ~ 1 °C that occurred when the vacuum pump is first turned on (Figure 2.5 (a)) followed by a slow rise back to a stable operating temperature. Since the membranes were exposed to butanol for a period of time before beginning the experiments, this rapid cooling most likely occurs from a high initial flux of butanol that is reduced as the membrane approaches a SS concentration profile. Expansion of gas in the permeate tube may also contribute to this initial cooling. Figure 2.5 (b) and (c) are directly adjacent in time, but are shown on two different time scales to illustrate the two distinct dynamic regions that occur following the addition of laser irradiation (at $t=2$ h). There is an initial logarithmic rise in membrane temperature and an apparent stabilization after ~ 2 min when the data is viewed on a small timescale (Figure 2.5 (b)). It is evident from Figure 2.5 (c), however, that there is a secondary logarithmic rise in temperature that can be seen when the subsequent data is viewed on an expanded timescale. This temperature rise stabilizes ~ 1 h after laser irradiation begins.

This result suggests that there are two separate heat transfer time constants (ratio of thermal mass to heat transfer rate, discussed in Chapter 3) associated with this system that control the dynamic response to laser irradiation. The time constants are represented by two different thermal masses: 1) the membrane/stainless steel mesh and 2) the butanol and cell walls adjacent the membrane. The thermal mass of the latter would greatly exceed that of the former

resulting in a much slower rise to a SS ΔT as is observed in the data. The respective time constants dominate at different times because of the time needed for the temperature change of the membrane to penetrate into the stagnant butanol. The gradual penetration of heat into the butanol may actually result in a dynamically growing thermal mass and thus an even slower approach to SS.

Figure 2.6 shows the final SS ΔT for each membrane during pervaporation as a function of incident laser power. Each value represents the difference in membrane temperature between a 1 h period leading up to turning on the laser and a 1 h period beginning 1 h after the laser is turned on (when SS is reached). The error bars show one standard deviation in 60 measurements over the 1 h period. The data show that the average SS ΔT increases as a function of Au content and exhibits a linear response to increasing laser power. Although SS ΔT increases linearly, the increases are typically less than proportional to the amount of additional incident laser power – i.e., the SS ΔT per W incident laser power decreases for each membrane at higher powers. Several factors exist that could contribute to this result (e.g., transduction efficiency, heat transfer parameters, etc.). This will be discussed in detail in the thermal modeling section of Chapter 3. There is a large increase in SS ΔT when AuNCM Au content is increased from 0.1% to 0.4%, but only a very small increase from 0.4% to 0.6%, despite a 50% increase in added Au and a significantly larger laser extinction fraction (Figure 2.2). This result suggests that, at higher concentrations, Au is not being used as efficiently to create additional 532 nm light-absorbing AuNPs. This observation will be examined in detail in Chapter 4.

2.3.2 Flux Enhancement

Laser irradiation of AuNCMs in the plasmonic pervaporation system resulted in stable, linear flux enhancements up to 117% that increased according to membrane Au content and laser

power. The butanol fluxes as a function of time for all membranes and values of incident laser power for the entire duration of the pervaporation experiments are shown in Figure 2.7. The data have been smoothed (boxcar 3) and shifted in time such that the laser is turned on at $t=0$ h for all data sets. After the laser is turned on, there is a 1-1.5 h dynamic region before a steady flux is reached, corresponding to the dynamic regions outlined in Figure 2.5 (b) and (c). There is a large amount of variability in the beginning fluxes of the membranes when the experiments begin caused by differences in the initial saturation state of the membranes. As the experiment proceeds, all the data sets approach a similar flux ($\sim 0.25 \text{ kg m}^{-2} \text{ h}^{-1}$) before the laser is turned on at $t=2$ h. As the figure shows, each data set demonstrates very stable performance throughout the operating period following the transition region. The flux increased for each set according to the Au content of the membrane and the incident laser power.

The average flux for each data set over the 5-10 h period of the pervaporation experiments is shown in Figure 2.8 (a). Error bars represent one standard deviation of 15 flux readings taken over 5 h (no smoothing). The variation in fluxes at 0 mW stem from minor differences in ambient conditions and small variances in membrane permeance (discussed in the following section). The flux for each membrane increases with increasing laser power. The rate of increase depends on the amount of Au content in the membrane. This effect is illustrated in Figure 2.8 (b) as the fractional increase in flux as a function of laser power relative to the same membrane under no irradiation. The lines in Figure 2.8 (b) show linear regressions of each data set. Flux enhancement is highly linear ($R^2 > 0.99$) over this range of temperatures for each membrane with slopes that rise according to Au content. The increase in slope slows logarithmically for the more highly concentrated AuNCMs indicating again that Au is being utilized less efficiently as more is added. The fluxes enhancement ranges from 16.9-47.6% for

the 0.0% membrane to 39.5-116.6% for the 0.6% membrane. This result demonstrates that the addition of plasmon-heated AuNPs to pervaporation membranes enables significantly higher flux enhancement from laser irradiation and that this enhancement increases according to the amount of added Au. These enhancements are accomplished with only moderate increases in feed temperature that fall quickly with increasing distance from the membrane (discussed in Chapter 3) which indicates partial realization of the hypothesized energy reduction.

2.3.3 Solution Diffusion Model

Examination of the fluxes and enhancements in Figure 2.8 (a) and (b) reveals two interesting observations: 1) flux of the 0.1% AuNCM at 0 mW is smaller than the 0.0% membrane despite a higher operating temperature and 2) the flux and enhancement are consistently larger in the 0.6% AuNCM than the 0.4% despite negligible differences in operating temperature (Figure 2.6). Both observations can be explained by investigation of the permeance of each membrane. To evaluate the membrane permeance, the effects of the driving force and permeance on butanol flux must be uncoupled. The *in situ* membrane thermal analysis offered by the plasmonic pervaporation system facilitated the direct determination of the AuNCM permeance using the solution diffusion (SD) model for membrane transport.

Membranes with pore sizes on the order of 5 Å or less are typically not described using the conventional pore model of membrane transport. At this point, pore size is on the order of the thermal motion of the polymer chains that compose the membrane and permeation is no longer pressure driven. Rather, it becomes a diffusive process controlled by the motion of the polymer chains.⁵⁹ Mass transport in membranes of this type is governed by three fundamental processes: 1) solution of molecules on the feed side of the membrane, 2) diffusion of molecules through the membrane, and 3) desorption of molecules on the permeate side of the membrane.

The SD model is most often used to describe this process.²² There are three key assumptions implicit in the SD model:

1. The fluid on each side of the membrane is in equilibrium with the membrane material at the membrane/fluid interface. Thus, the component chemical potentials are equal in the membrane and fluid phases at each interface and there is a continuous gradient between them.
2. Absorption and desorption occur much faster than diffusion through the membrane and can therefore be neglected.
3. Pressure throughout the membrane is assumed to be equal to the feed pressure and therefore transport is governed solely by the concentration gradient across the membrane.

These assumptions result in a Fick's law diffusive flux:

$$J_i = D_i \frac{dc_i}{d\ell} = \frac{D_i}{\ell} (c_{i,0(m)} - c_{i,\ell(m)}) \quad (2.2)$$

where J_i is the molar flux of i (equal to j from eq 2.1 divided by molecular weight), D_i is the diffusivity of i in the membrane, ℓ is the length of the membrane, and $c_{i,0(m)}$ and $c_{i,\ell(m)}$ are the concentrations of i in the membrane on the feed side and permeate side, respectively. Since component concentrations in the membrane phase are difficult to obtain, they must be determined in terms of fluid phase concentration by setting the respective chemical potentials equal (assumption 1 above) and solving. From this point, the SD model can be applied to a variety of membrane operations (e.g., reverse osmosis, gas separations) including pervaporation.⁶⁰

The pervaporative flux of a component, i , according to the SD model and written in terms of fluid phase concentrations (partial pressure for the vapor phase) is

$$J_i = \frac{D_i}{\ell} (K_i^L c_{i,0} - K_i^G p_{i,\ell}) \quad (2.3)$$

where K_i^L and K_i^G are the liquid and gas phase sorption coefficients, respectively, representing the ratio of component i 's activity coefficients in either the liquid and gas phase to that in the membrane phase, $c_{i,0}$ is the concentration in the feed, and $p_{i,\ell}$ is the partial vapor pressure of i in the permeate. The sorption coefficients are for different phases and differ slightly in definition; thus K_i^L is dimensionless and K_i^G has units of concentration divided by pressure. The full derivation of these parameters is given by Wijmans⁶⁰

The different sorption coefficients make this form of the SD model unwieldy from a practical standpoint. This difficulty is overcome by considering a hypothetical vapor in equilibrium with the feed liquid. Equating the chemical potential of these two phases enables redefining the liquid phase concentration in terms of partial vapor pressure

$$c_{i,0} = \frac{K_i^G}{K_i^L} p_{i,0} \quad (2.4)$$

where $p_{i,0}$ is the partial vapor pressure i in the hypothetical vapor phase in equilibrium with the feed liquid. Substituting eq 2.4 into 2.3 and rearrangement yields

$$J_i = \frac{D_i K_i^G}{\ell} (p_{i,0} - p_{i,\ell}) \quad (2.5)$$

The product, $D_i K_i^G$, is referred to as the gas phase permeability coefficient, P_i^G . When the permeability is weighted by the membrane length, it becomes the membrane permeance, \overline{P}_i :

$$\overline{P}_i = \frac{P_i^G}{\ell} = \frac{D_i K_i^G}{\ell} \quad (2.6)$$

It is important to note that the equilibrium interaction of a sorbed vapor in the liquid phase with the partial pressure of the vapor is given by Henry's law:

$$p_{i,0} = H_i c_{i,0} \quad (2.7)$$

where H_i is the Henry's law coefficient in units of pressure divided by concentration. From eq 2.4, it follows that

$$H_i = \frac{K_i^L}{K_i^G} \quad (2.8)$$

and eq 2.5 can be returned to a concentration-based driving force as⁶⁰

$$J_i = \bar{P}_i (c_{i,0} H_i - p_{i,\ell}) \quad (2.9)$$

2.3.4 AuNCM Permeance

Rearrangement of eq 2.5 allows the gas phase permeance of the AuNCMs to be calculated using experimental flux and driving force data:

$$\bar{P}_i = \frac{J_i}{p_{i,0} - p_{i,\ell}} \quad (2.10)$$

In the single component system used in this work, $p_{i,0}$ and $p_{i,\ell}$ are equal to the saturation vapor pressure of butanol at the membrane temperature and the total permeate pressure, respectively. The permeance of each AuNCM at each level of laser power was computed according to eq 2.10 by calculating the saturation vapor pressure from the measured membrane temperature during operation.

At 0 mW laser irradiation, the permeance of each membrane was 1.07, 0.93, 1.07, and 1.09 mol h⁻¹ m⁻² torr⁻¹ for the 0.0, 0.1, 0.4, and 0.6% membranes, respectively. Remarkably, the membranes demonstrate very consistent base (no irradiation) permeance values. The 0.1% AuNCM varies more and appears to be an outlier in this regard, but still only varies from the average of the remaining three membranes by <14%. The lower value of permeance explains the first observation made in the beginning of section 2.3.3 – that the flux of the 0.1% AuNCM is

lower at 0 mW than the 0.0% membrane despite a slightly higher operating temperature. Eventually, the 0.1% flux is enhanced beyond that of the 0.0% as incident radiation is increased due to increased heat generation from the presence of the AuNPs.

The second observation from section 2.3.3 can be explained by evaluating how the permeance values for each membrane change as a function of temperature. Although little variation is seen in the 0 mW permeance values of the membranes, as temperature is increased (increased laser irradiation), the values vary widely. Figure 2.9 shows the fractional change in permeance for each membrane as a function of temperature change. The permeance falls linearly with increasing temperature for each membrane, but the rate at which it falls decreases with increasing Au content. The 0.6% AuNCM appears to exhibit higher flux values and enhancements than the 0.4% AuNCM at similar SS ΔT s (i.e., driving forces) because it maintains a higher permeance at elevated temperatures. A pervaporation activation energy analysis is typically used to decipher how temperature changes affect membrane permeance.⁶¹ This analysis, as well as a hypothesized explanation for the mitigation in permeance reduction with increasing Au content, is given in Chapter 3.

2.4 CONCLUSIONS

For the first time, a plasmonic pervaporation system was designed and constructed. The system enabled uniform laser membrane excitation, full thermal analysis of membrane surface temperature during operation, and automated operation and data capture (flux, membrane and feed temperature, permeate pressure, and ambient conditions). Novel AuNP-functionalized PDMS membranes were fabricated in varying concentrations (0.0, 0.1, 0.4, and 0.6% Au by mass) and were tested for performance in the plasmonic pervaporation system against a bare PDMS membrane at four levels of laser irradiation (0, 250, 500, and 750 mW). Laser irradiation

resulted in stable enhancement of butanol fluxes up to 117% that increased according to both Au content in the membrane and laser power. The membrane thermal analysis offered by the system enabled calculation of membrane permeance using the solution diffusion model. It was observed that the permeance of each membrane fell with increasing temperature, but the reduction rate (as a function of temperature) decreased with increasing Au content.

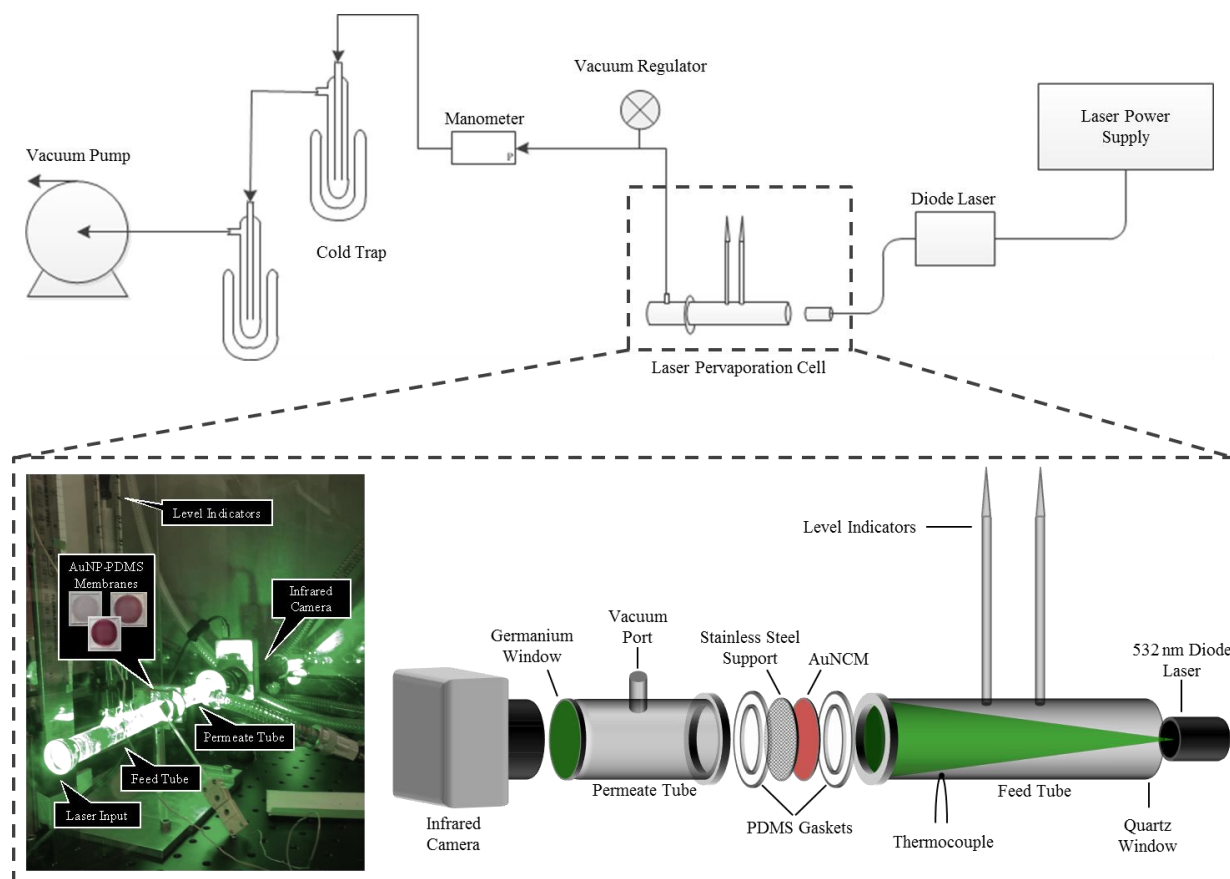


Figure 2.1. Schematic of the experimental plasmonic pervaporation system and the laser excited pervaporation cell. Image shows plasmonic pervaporation cell during operation.

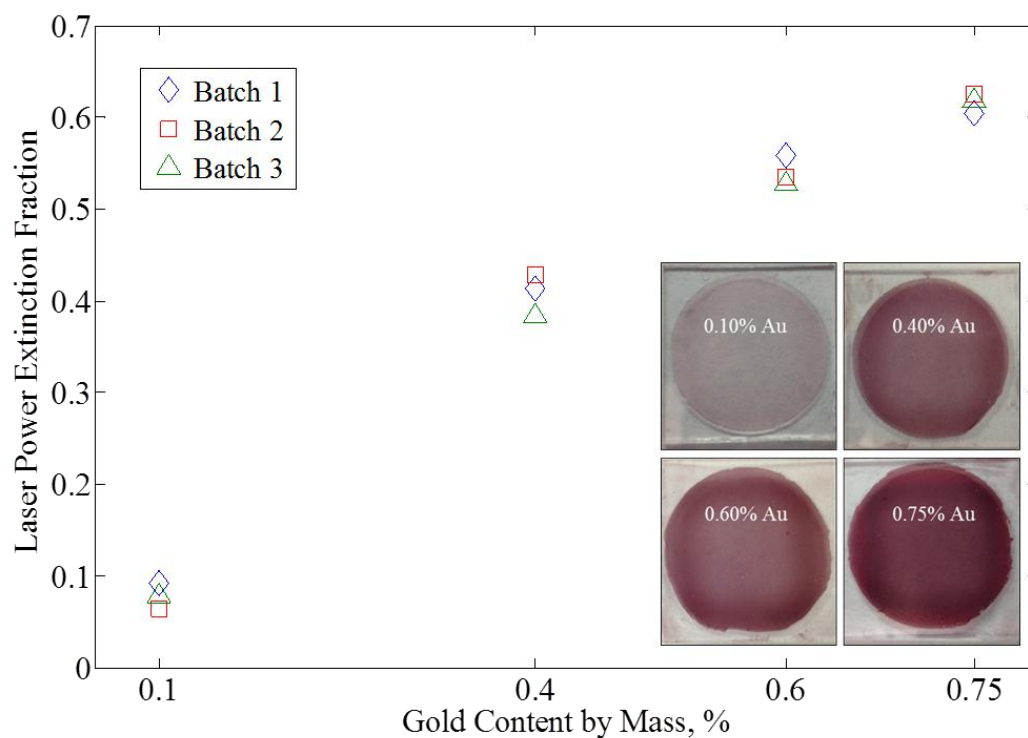


Figure 2.2. Values of laser power extinction fraction (532 nm) for AuNCMs from three different batches at four different values of gold content. Each AuNCM is pictured in the inset. Extinction fractions of the glass substrate and bare PDMS were measured independently and have been factored out of the values in the figure – therefore a 0.0% Au membrane has an extinction fraction of zero on this scale.

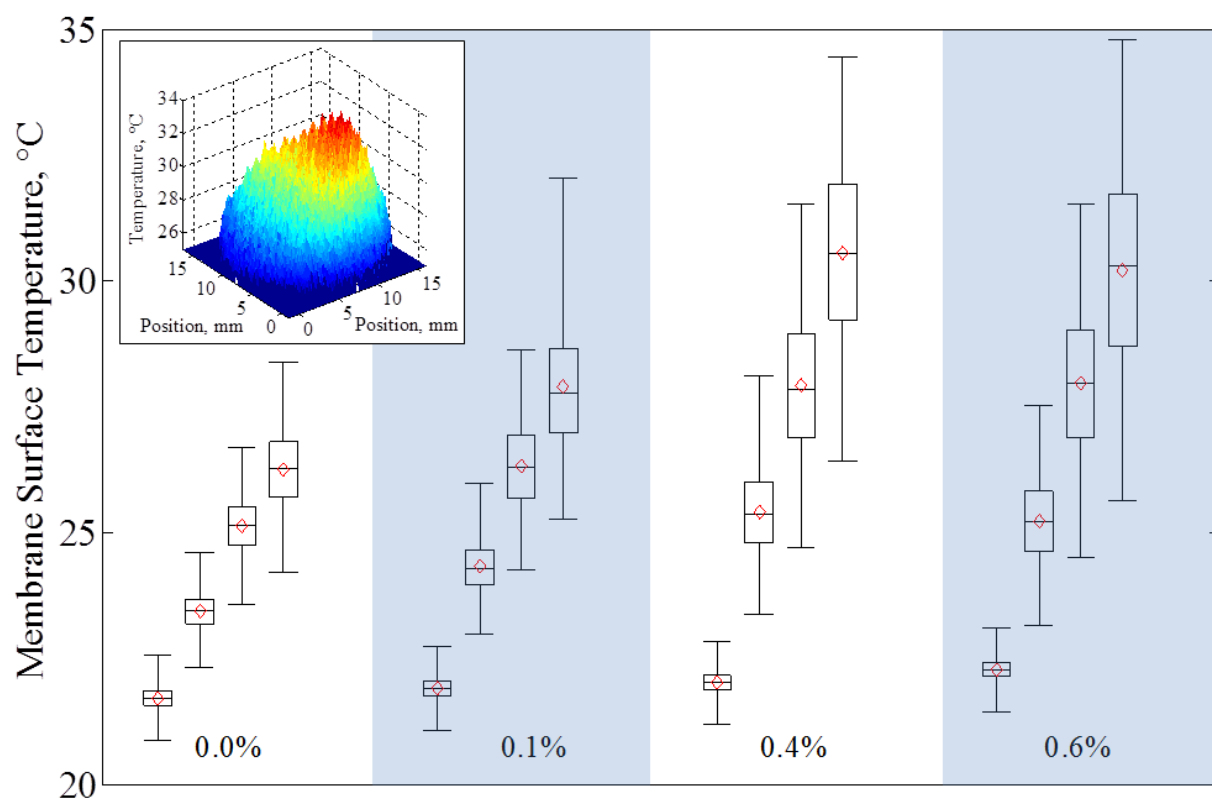


Figure 2.3. Box and whisker plots of membrane thermal distributions during the 5-10 h period of pervaporation experiments for the four membranes (0.0, 0.1, 0.4, and 0.6% Au) at four levels of laser irradiation (left to right, 0, 250, 500, and 750 mW). The mean temperature for each point is also shown (red diamonds). Inset shows a representative spatial thermal distribution across the membrane.

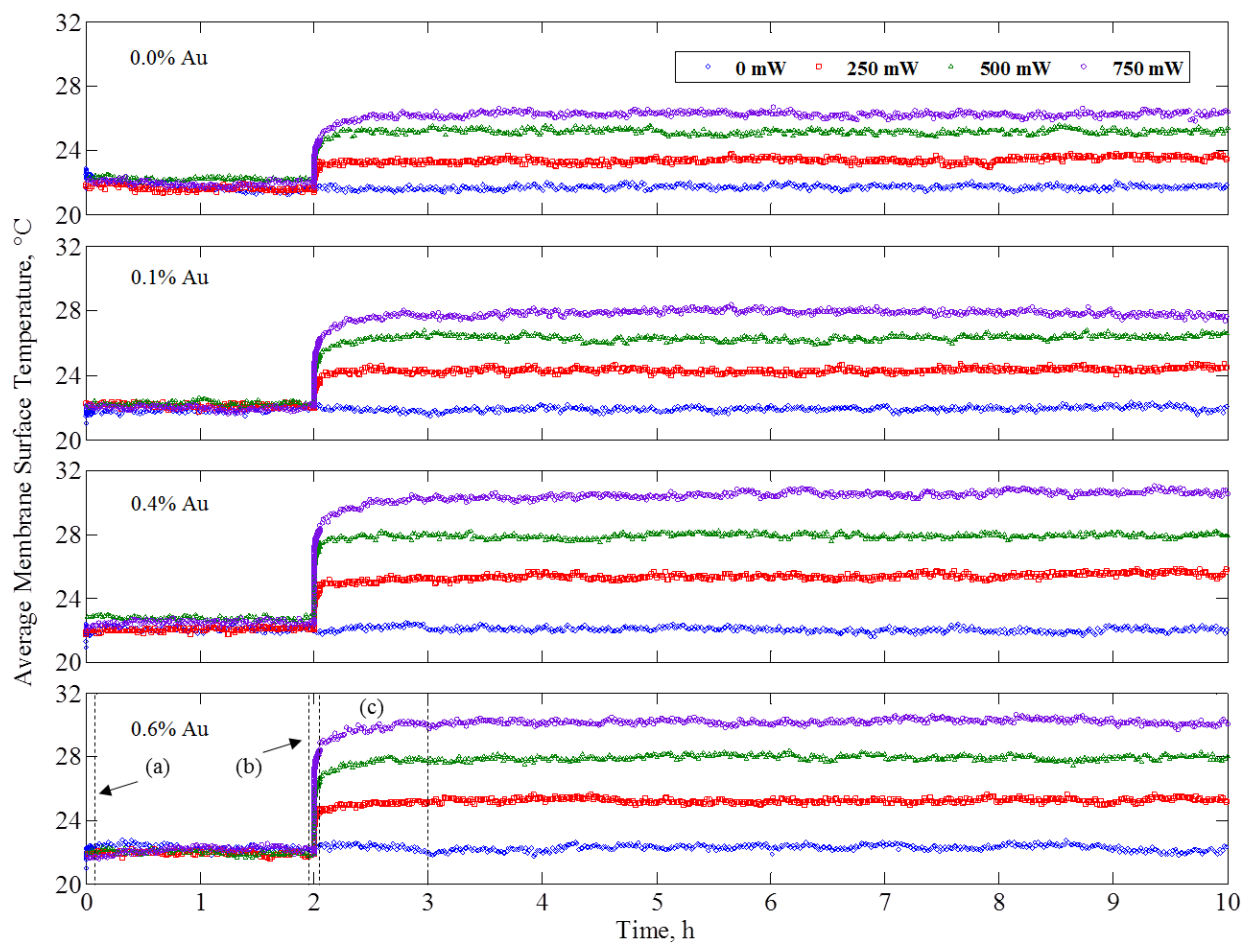


Figure 2.4. Average membrane surface temperature with time for the 0.0, 0.1, 0.4, and 0.6% Au membranes irradiated with 0, 250, 500, and 750 mW laser power during butanol pervaporation experiments. Regions (a), (b), and (c) in the 0.6% graph indicate dynamic thermal regions that are illustrated in Figure 2.5.

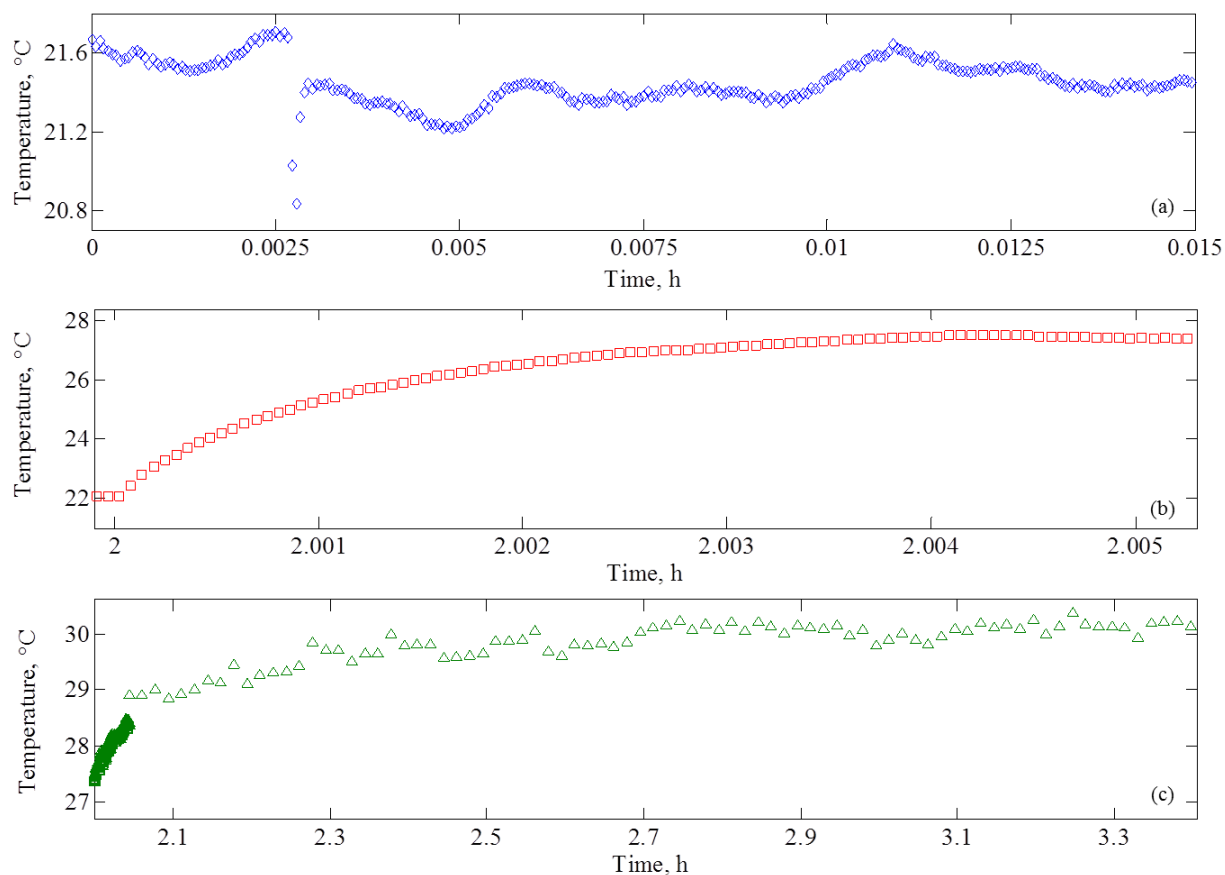


Figure 2.5. Average temperature of a 0.6% AuNCM with time during the three dynamic thermal regions of the plasmonic pervaporation experiments (750 mW laser irradiation): (a) when the pump is turned on (diamonds), (b) when the laser is turned on and the thermal mass of the membrane dominates (squares), and (c) region after turning on the laser in which the thermal mass of butanol and the cell wall dominate (triangles). Regions (a), (b), and (c) correspond to those indicated in Figure 2.4.

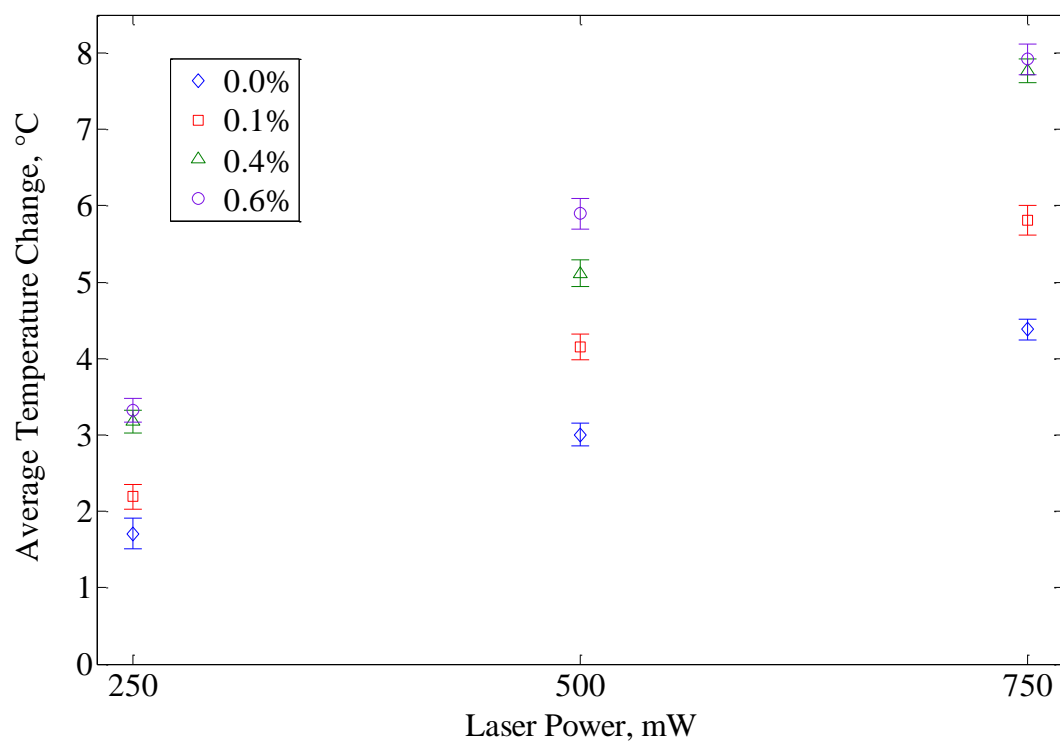


Figure 2.6. The average steady state temperature change during butanol pervaporation for membranes of different Au content as a function of incident laser power. Error bars show one standard deviation of 300 measurements taken over the period of 5 h.

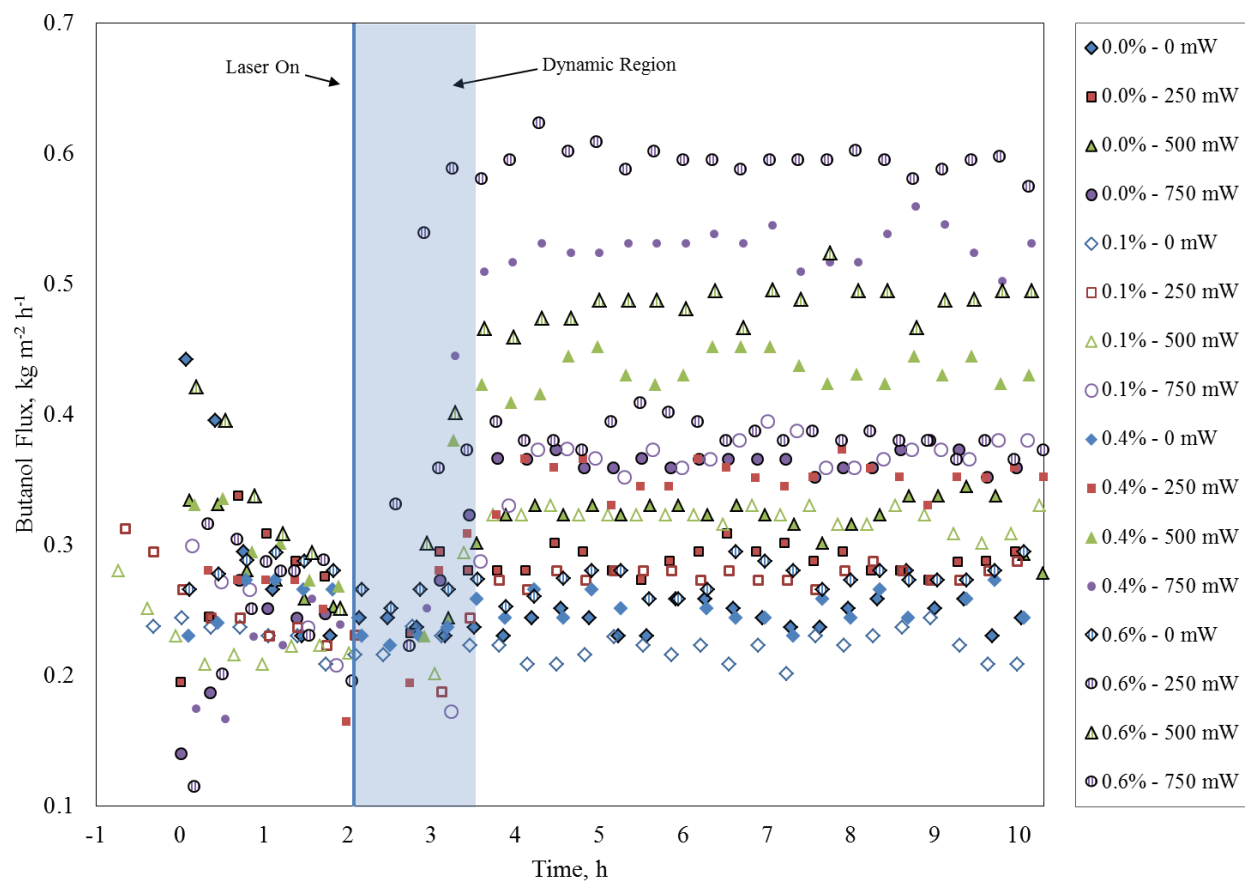


Figure 2.7. Flux of butanol as a function of time for the four membranes with varying incident laser powers. The data points have been smoothed (boxcar 3) and shifted in time such that the laser is turned on at $t=2$ h. A dynamic region (shaded) follows $t=2$ h during which steady state is reached.

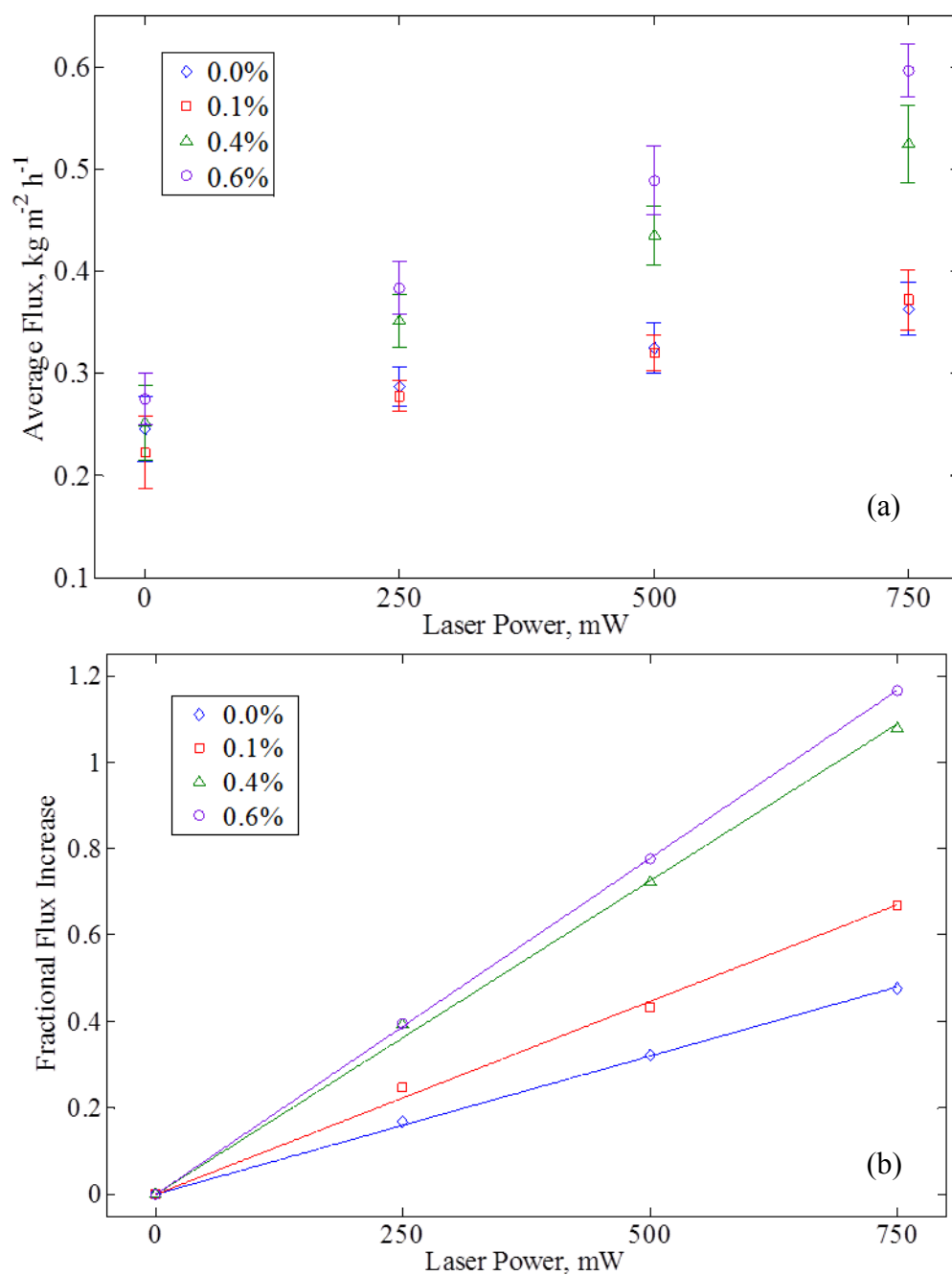


Figure 2.8. (a) Flux of butanol as a function of incident laser power. Error bars represent one standard deviation of 15 flux readings taken over a 5 h period. (b) The fractional increase in flux as a function of incident laser power. Lines in (b) represent least squares regressions of the data.

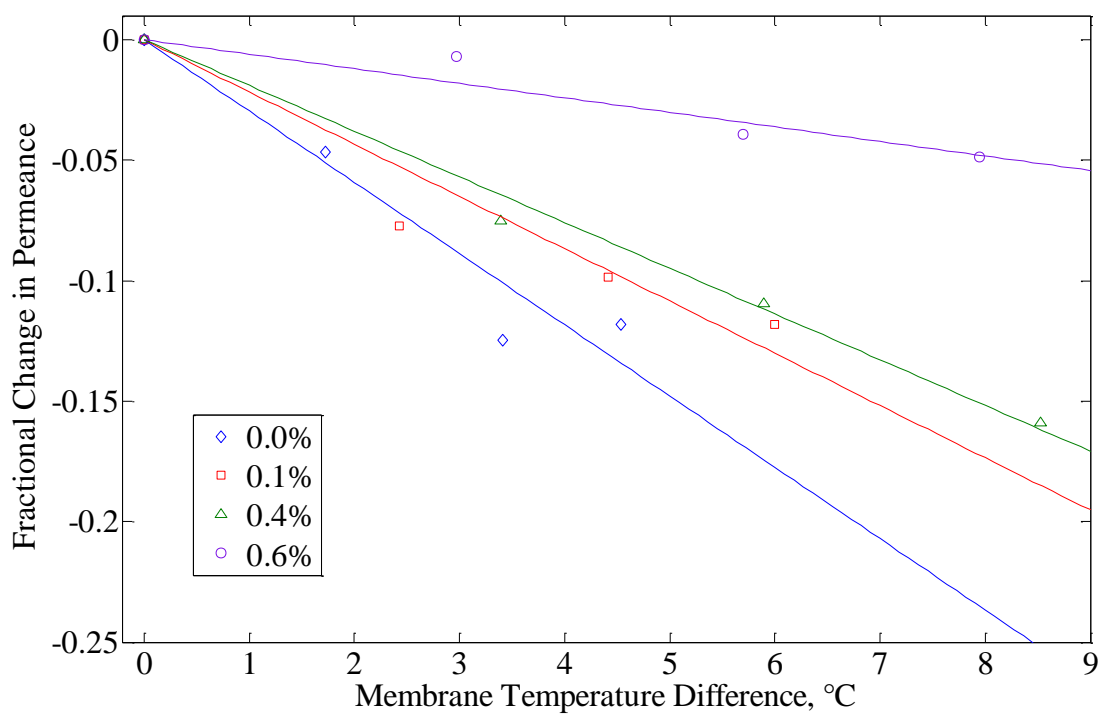


Figure 2.9. Fractional change in permeance as a function of membrane temperature change for the four membranes studied. Lines represent linear regressions of each data set.

CHAPTER 3

MODELING PLASMONIC PERVAPORATION

3.1 SIGNIFICANCE OF THE PRESENT WORK

In order to achieve the highest economic impact in plasmonic pervaporation, it is necessary to identify the means by which the laser energy input is consumed. The ideal case discussed in Chapter 1 assumed 100% of the laser energy was absorbed by the membrane and that it all was consumed by evaporating permeate. The purpose of this chapter is to quantify the thermal behavior of the plasmonic pervaporation system at steady state and to evaluate the extent to which the ideal case is realized in this system. In the first section, a previously demonstrated model for plasmonic heating is adapted to describe the thermal behavior of the AuNCMs in operation. In the second section, a pervaporation activation energy analysis is used to develop an empirical model that accurately describes the experimental data and can be used to estimate flux enhancement at temperatures beyond those measured experimentally. In the final section, these two models are coupled to predict the performance of the plasmonic pervaporation system under conditions matching those used in the preliminary economic analysis to evaluate its realization.

Considerable experimental and computational work has been done to measure and predict the thermal and optical behavior of AuNPs under high-power, pulsed laser irradiation with large temperature increases in aqueous solutions⁶²⁻⁶⁸ as well as in live cells.^{69, 70} In Roper's lab in particular, as well as some others, thermal behavior of aqueous AuNP/media and solid-state

AuNP/substrate systems as a whole have been examined under relatively low steady state temperature increases by continuous wave excitation.^{44, 71-73} However, as no other system of this type has been developed, quantitative description of thermal energy transfer has not been performed.

3.2 THERMOPLASMONIC MODELING

3.2.1 Capillary Thermal Model

The model to describe the plasmonic pervaporation thermal behavior was adapted from a previously developed model for plasmonic heating in open, fluid-filled AuNP-plated silica capillaries.^{44, 72} The model was given by^{45, 74}

$$\frac{dT}{dt} = \frac{Q_I - \sum_i Q_{O,i} - \dot{m}\Delta H_{v,f}}{\sum_j m_j C_{p,j} + (m_f - \dot{m}t)C_{p,f}} \quad (3.1)$$

where the left hand side equals the changes in the uniform temperature of the system, T , as a function of time, t . The terms in the numerator on the right hand side represent, respectively, energy input from the laser, Q_I ; power losses due to conventional heat transfer modes, i.e. conduction, convection, and/or radiation, contained in the sum $\sum Q_{O,i}$; and power lost by evaporative cooling, $\dot{m}\Delta H_{v,f}$, which is the evaporation rate, \dot{m} , multiplied by the heat of vaporization of the fluid, $\Delta H_{v,f}$. The terms in the denominator represent the dynamic thermal capacity of the system in which $\sum m_j C_{p,j}$ is the sum of the masses of system components (e.g., the capillary) multiplied by their respective specific heat capacities, $C_{p,j}$, m_f is the initial fluid mass, and $C_{p,f}$ is the specific heat capacity of the fluid. This energy balance is illustrated in Figure 3.1. The surface temperature of the small capillary was considered uniform due to its short internal thermal equilibration time, resulting from high conductivity of Au and silica, relative to equilibration with its external environment.³⁹ This allows neglecting internal thermal resistances

in the energy balance and linear summation of power losses by convection, conduction, and/or radiation from a “black box” – illustrated by the dotted line in Figure 3.1– which has constant energy input via incident light.⁴⁵

The energy input term, Q_I , is the thermal energy transduced from the absorbed laser power and results from crystal lattice excitation (phonon) that occurs as optically-induced plasmons on the AuNP surfaces decay. This term was previously defined by Roper *et al.*⁷² as

$$Q_I = I(1 - 10^{-A_\lambda})\eta_T \quad (3.2)$$

where I is the incident laser power, A_λ is the measured AuNP spectral absorbance at the wavelength of excitation, λ , and η_T , is the transduction efficiency. The value, η_T , represents the fraction of absorbed laser power that is transduced to thermal energy. Measurement of transmitted laser light through the capillary during experimentation enables Q_I to be conveniently redefined as

$$Q_I = (I - I_T)\eta_T \quad (3.3)$$

where I_T is the measured transmitted laser power.

The term $\Sigma Q_{0,i}$ in eq 3.1 sums external thermal transfer modes not related to mass transfer: conduction, Q_{cond} ; convection, Q_{conv} ; and radiation, Q_{rad} . Conduction is given by

$$Q_{cond} = \frac{kA_c}{L}(T - T_{amb}) \quad (3.4)$$

where k is the thermal conductivity of the surface, A_c is the contact area perpendicular to conduction, L is the characteristic length for conduction to the environment, and T_{amb} is the ambient temperature. Power loss by convection is given by

$$Q_{conv} = h_{conv}A_s(T - T_{amb}) \quad (3.5)$$

where h_{conv} is the heat transfer coefficient for convection and A_s is the surface area of the sample cell exposed to air. Radiation power loss is given by

$$Q_{rad} = A_s \epsilon \sigma (T^4 - T_{amb}^4) \quad (3.6)$$

where ϵ is the emissivity of AuNPs and σ is the Stefan-Boltzmann constant.

The mass transfer rate of liquid from the capillary to the ambient environment is given by

$$\dot{m} = A_E MW_f k_c \Delta C_f \quad (3.7)$$

where A_E is the area available for evaporation, MW_f is the molecular weight of the liquid, k_c is the mass transfer coefficient, and ΔC_f is the difference in liquid concentration between the liquid boundary and the environment. The mass transfer coefficient, k_c , was given by

$$k_c = \frac{N_A}{\Delta C_f} \quad (3.8)$$

where N_A is the experimentally determined average molar flux of the liquid from the substrate surface. Substitution of Eq 2.8 into Eq 2.7 gives an alternate definition of the mass transfer rate:

$$\dot{m} = A_E MW_f N_A \quad (3.9)$$

The model was tested experimentally using a AuNP-silica nanocomposite capillary fabricated by electroless plating and thermal annealing technique^{75, 76} The model was shown to accurately predict the dynamic and steady state thermal behavior of the capillary over a defined range of conditions including evaporation of organic and aqueous liquids.^{45, 74} Although, it was developed to describe the capillary system shown in Figure 3.1, the generality it possesses enables its extension to any system that conforms to the constraints discussed herein – i.e., linearly additive heat transfer modes to and from a defined system (black box) at a uniform temperature. The following section discusses extension of this model to the plasmonic pervaporation system.

3.2.2 Plasmonic Pervaporation Model

For the plasmonic pervaporation system, the system was defined as the AuNCM and stainless steel mesh. The system has a single heat input from the laser and all heat output occurs axially into either the feed or permeate tube. A schematic illustrating heat transfer to and from the membrane/mesh system is given in Figure 3.2. On the permeate side, four modes of heat loss are identified. They include: 1) temperature rise of the permeate (it was assumed to evaporate at the temperature of the membrane), 2) heat of vaporization from permeate, 3) heat of isothermal expansion from atmospheric pressure to permeate pressure (previously demonstrated to be significant²⁴), and 4) radiation from the membrane/mesh surface. Conduction and convection are taken to be negligible on the permeate side due to the low pressure (2 torr). On the feed side, heat transfer is taken to occur only by conduction into the feed liquid. Conduction into the feed liquid is difficult to determine because the characteristic length (eq 3.4) is not readily definable. However, at steady state, all heat transferred to the feed liquid will be transferred to the environment via convection and conduction from the feed tube walls. Because of the geometry of the system (heat conduction from a hot surface through a long, cylindrical tube), heat transfer from the feed tube walls is estimated using a relation for an infinite fin. In the following section, the assumptions and possible sources of uncertainty associated with this approach are discussed.

This approach yields the following relation for membrane/mesh temperature as a function of time:

$$\frac{dT}{dt} = \frac{Q_I - Q_{fin} - Q_{rad} - \dot{m}(C_{p,f}(T - T_{amb}) + \Delta H_{v,f} + q_{exp})}{\sum_j m_j C_{p,j}} \quad (3.10)$$

where Q_I is the power input from the laser, Q_{fin} is the power loss from the feed tube (defined below), Q_{rad} is the power loss due to radiation to the permeate side (defined by eq 3.6). The

power loss from evaporation of butanol permeate is calculated by the product of the mass evaporation rate, \dot{m} , and the sum of i) the product of the heat capacity of butanol and the temperature change, ii) the heat of vaporization, ΔH_{vf} , and iii) the heat generation per mass of isothermally expanded material, q_{exp} . The thermal mass (denominator) of the plasmonic pervaporation system is convoluted by the multiple time constants discussed in Chapter 2. Thus, in this study, only steady state operation was investigated because the thermal mass has no bearing on the steady state behavior, only the time it takes to reach it. In order to predict the transient behavior of the system, the transient penetration of heat into the feed liquid could be modeled using a semi-infinite medium relation, but that analysis is beyond the scope of this work.

The rate of heat transfer from an infinite fin is given by⁷⁷

$$Q_{fin} = \sqrt{h_{fin} p k_{fin} A_{fin}} (T_b - T_{amb}) \quad (3.11)$$

where h_{fin} is the heat transfer coefficient (combining effects of convection and radiation), p is the perimeter of the fin, k_{fin} is the thermal conductivity of the fin, A_{fin} is the cross-sectional area of the fin, and T_b is the temperature of the fin base, taken to be the membrane temperature. The area for radiation in eq 3.10 was assumed to be the exposed area of the membrane plus 80% of the surface area of the stainless steel since the feed-facing side of the mesh is in contact with the membrane. This parameter is difficult to identify, but a variation in its value from 60-100% only has an effect of $\sim \pm 2\%$ on overall heat transfer from the system. The heat generated per mass due to isothermal expansion of an ideal gas was defined as⁷⁸

$$q_{exp} = -RT \ln \left(\frac{P_2}{P_1} \right) \quad (3.12)$$

where R is the gas constant and P_1 and P_2 are the pressures on the feed and permeate sides, respectively.

3.2.3 Accuracy of Infinite Fin Approach

Use of the 1-dimensional infinite fin model to calculate power loss through the feed liquid introduces several potentially significant uncertainties due to certain assumptions that have been made. These assumptions include: 1) a uniform butanol temperature across the radius of the fin and 2) free convection-dominated fin heat loss. The first assumption is expected to result in some uncertainty because the base temperature, T_b , in the model is assigned to be the average membrane temperature taken to be uniform throughout the membrane. Since the measured membrane temperatures were nonuniform with a substantial distribution (Figure 2.3), using this assumption could overestimate fin heat transfer because actual temperatures changes less sharply than model fin temperatures toward the perimeter. The second assumption may also introduce uncertainty in the approach since radiation can, at times, dominate heat transfer in free convection environments.⁷⁷ Below, evidence is provided to support the use of this approach as a first approximation despite these potential uncertainty.

To evaluate the accuracy of the infinite fin approach, the steady state exterior temperature of the feed tube for each data set, measured by the thermocouple (Figure 2.1), was compared to temperatures calculated for the same position using the infinite fin model. This comparison assumes there is a negligible temperature drop across the glass to where temperature is being measured by the thermocouple. This assumption should introduce little uncertainty as the thermal conductivity of the glass is nearly an order of magnitude larger than that of butanol and the glass is thin (~3 mm). The thermal profile as a function of distance away from the base is given by⁷⁷

$$T(x) = T_{amb} + (T_b - T_{amb}) \exp\left(-x \sqrt{\frac{h_{fin} p}{k_{fin} A_{fin}}}\right) \quad (3.12)$$

where $T(x)$ is the fin temperature at distance x ($x=0$ at fin base). For the predicted temperatures, the average membrane temperature was used for T_b , x was 1.7 cm, h_{fin} was calculated for each data set (because it depends on SS ΔT) using a free convection model for cylindrical tubes using ambient conditions,⁷⁷ p and A_{fin} were measured, and k_{fin} was taken as an average of the thermal conductivities of glass and butanol (weighted by their fractional contributions to the A_c).

The calculated and measured temperatures are shown in Figure 3.3. There is excellent agreement between the calculated and measured temperatures for each data set, excluding the 0.1% AuNCM. The temperatures vary considerably more for this membrane than for the others. Because all data was taken under the same conditions, the large difference is most likely a result of experimental error. There were times during experimentation when the thermocouple was detached from the feed tube and had to be reattached. It is possible that incorrect placement of the thermocouple could account for the temperature differences. The alignment of the remaining data sets is extraordinary. Measurement of additional thermal points along the cell may offer improved confidence in the thermal model.

3.2.4 Model Results

In general, the thermal model can provide a means of estimating both the average SS ΔT of the membrane and the power loss due to each mode of heat transfer according to three input parameters: the incident laser power, the laser absorbance fraction (product of extinguished laser light and transduction efficiency), and the experimentally measured (steady state) mass flux. In this work, the laser absorbance fraction of the membranes was unknown, but the SS ΔT were measured experimentally. This allowed an estimation of the laser absorbance fraction for each

data set to be made by manipulating its input value to achieve a SS ΔT that agreed with the experimental results. The resulting laser absorbance values are shown in Figure 3.4 – these values represent the absorbance of both the AuNCM and the stainless steel mesh. As the figure demonstrates, the laser absorbance fractions varied from a minimum of 0.066 for the 0.0% membrane at 750 mW to a maximum of 0.167 for the 0.6% AuNCM at 250 mW and, expectedly, the values increase consistently according to Au content of the membrane.

Several interesting observations can be made from the data in Figure 3.4. First, the absorbance values of the AuNCMs are much lower than their extinction fractions measured with the laser (Figure 2.2), especially for the higher Au content membranes. This difference could be attributable to a number of factors. Primarily, AuNCM extinction was measured under different conditions than those experienced during operation including a smaller laser spot size and different substrate. This prevents a direct comparison. Additionally, laser loss due to its path through the feed tube during operation was not present during extinction fraction measurements. Differences can also be attributed to the extinction contribution due to light scattering, rather than absorption, in the membranes. As was previously mentioned (section 1.2), AuNPs that absorb in the green wavelengths (532 nm) typically demonstrate transduction efficiencies near 100%. As AuNP diameter is increased, the scattering cross-section of the particles grows, exceeding the absorption cross-section.⁴³ This is a possible indication that large Au particles may be forming in the AuNCMs, resulting in an increase in scattering. This possibility is examined more closely in the following chapter. Lastly, because the absorbance fraction of the 0.0% membrane is on the order of all the AuNCMs (due to light absorbance by the mesh), the stainless steel mesh appears to make a large contribution to the absorbance at each laser power. Exactly how large a contribution it makes is difficult to estimate because of the dependence of

each absorbing element on the other – i.e., as the AuNCM absorbs more light, there is less available to be absorbed by the mesh.

The highest value of absorption calculated for the stainless steel mesh alone (0.0% Au content) was 9.9% at 750 mW. Based on its measured cross sectional area (41.9% of the active membrane area) and the experimental absorption values for stainless steel reported in one study (40-65%),⁵⁸ the absorption fraction could be expected to be as high as 16.8-27.2%. This result could possibly indicate that the heat absorbed by the membrane is being underestimated by the model. This cannot be determined with certainty considering the absorption values in the cited study varied considerably with steel type and the exact make of the mesh is unknown. However, it does help to stress the convolution of model results that occurs due to the absorption by the mesh. In future work, it would be beneficial to devise a mechanical support that is optically inert.

Another interesting result from Figure 3.4 is that the absorbance fraction falls for each membrane with increasing laser power. The overall drop is significant from 250-750 mW – 32.9, 26.0, 26.6, and 27.6% for the 0.0, 0.1, 0.4, and 0.6% membranes, respectively – but it appears to slow with increasing power. This reduction in absorption could be attributed to multiple factors including actual changes in the absorbance properties of the system and/or underestimation in the model regarding heat transfer modes that increase nonlinearly with increasing temperature. Review of the literature suggests the former is less likely given that only minor decreases in AuNP extinction have been observed with >50 °C temperature increases⁷⁹ and the absorption of light by metals (the stainless steel) is generally shown to increase with increasing temperature.⁵⁸ However, the exact absorption properties of steel, particularly its continuous wave laser absorption capacity, and how they change with increased irradiation is unknown. Also, we have

observed that absorbance fractions of AuNP-silica nanocomposites under lower irradiation powers^{44, 74} and extinction fractions of AuNCMs under similar irradiation powers do not vary measurably. However, the conditions of these experiments were notably different from those experienced in the plasmonic pervaporation system and therefore cannot preclude the possibility of actual changes in the absorbance behavior of the membranes. The location of the AuNPs in a thermally insulating environment (low conductivity, radiation) may result in partial saturation of the plasmon resonance capacity due to the increasing requisite time for phonon transfer. Because a similar effect is seen with the 0.0% membrane, this effect could only partially account for the loss in absorption efficiency.

Because the absorption values fall so much, if underestimations in one or more heat transfer modes occurred, they would need to be significant in the overall thermal behavior of the system. Table 3.1 gives the contributions of each heat transfer mode calculated by the model for each data set. A majority (77-79%) of the input power is dissipated by conduction to the feed (Q_{fin}) and vaporization of the permeate. These power losses are similar at lower temperatures, but conduction increasingly dominates as temperature increases. Power loss from permeate evaporation is set by the flux rate and therefore is not considered to contribute significantly to potential underestimation. Power loss from radiation and expansion account for the vast majority of the remaining power loss and follow a similar trend with radiation dominating as temperature increases. Radiation from the feed side of the membrane was not considered and could be significant depending on the infrared absorption characteristics of butanol. Thus, if underestimations were made, they could most likely be attributed to any combination of the remaining three modes, all of which have the potential to be nonlinear in their dependence on

temperature (free convection heat transfer coefficient, radiation driving force, non-ideal gas expansion).

Feed conduction in the model was determined by the fin relation and is set by the system geometry, thermal conductivity, and the free convection heat transfer coefficient. As a function of increasing temperature change, the free convection heat transfer coefficient increases in a logarithmic-type profile – quickly at first but slowing as the temperature change grows. This profile is similar to that which would be required to induce the slowing loss in absorption efficiency as mentioned above. The coefficients calculated in the model are on the order of $5 \text{ W m}^{-2} \text{ K}^{-1}$. Since the values are so small, an underestimation of only several $\text{W m}^{-2} \text{ K}^{-1}$ could account for significant differences in the calculated power loss to the feed. Measurement of additional thermal points along the length of the feed cell would reduce uncertainty in the feed heat loss prediction in future experiments.

Although there is the possibility of uncertainty in the thermal model, it provides a useful approximation of how effectively the input energy is being consumed as well as indicating how it may be improved. In the ideal case for plasmonic pervaporation, all laser energy is absorbed by the membrane and used explicitly for the evaporation of additional permeate. In reality, laser absorption is limited by the absorbance fraction of the membrane and some heat will be lost by alternate mechanisms. The blue diamonds in Figure 3.5 show the percentage of incident light that is consumed by the vaporization of butanol for each membrane at 250, 500, and 750 mW laser irradiation (left to right). For all membranes, each value falls below 7%, due mostly to the low absorbance fraction. The red squares show the same data on the basis of absorbed light rather than incident light. These values show that if 100% absorption was achieved in the AuNCMs, >40% of the energy could be channeled to vaporization of the permeate. The

percentages fall with increasing laser power due to the combined effects of increased conduction to the feed and decreased absorption fraction.

The thermal model shows that these two factors, heat loss to feed and absorption efficiency, will exhibit the largest control over energy efficiency in the plasmonic pervaporation process. Improvement in either factor would increase the overall economic impact. However, the results in Figure 3.5 suggest that a much larger impact is possible by focusing on the improvement of AuNCM light absorption. Independently reducing heat loss to the feed to 0% or alternatively increasing AuNCM absorption efficiency to 100% result in 1.6- to 3-fold or 6.4- to 12-fold reductions in energy demand, respectively. In the following section, an empirical model is developed that can be used in conjunction with this thermal analysis to predict the economic impact of this process based on the initial analysis given in section 1.4.

3.3 PERVAPORATION MODELING

The economic impact analysis used a basis of a system with a 37 °C feed heated to 70 °C for pervaporation. Based on the study used for the basis,¹⁹ flux was enhanced by a factor of 4.9 due to the increase in temperature. In order to estimate the economic effect of plasmonic heating on the same basis, we must be able to estimate the energy input required to achieve an equivalent flux enhancement. The effect on flux of increased driving force is readily calculated from the vapor pressure as a function of temperature, but the effects of membrane permeance must be modeled empirically using an activation energy analysis of the experimental fluxes. This analysis also provides insights into why the permeance of the AuNCMs fell with increasing temperature at rates that decreased according to Au content as was shown in Figure 2.9.

3.3.1 Activation Energy Analysis

Membrane permeance is dependent on both the diffusivity and sorption coefficients of components in the membrane phase (eq 2.6). Temperature dependence of both these parameters can be expressed as an Arrhenius-type relationship:⁶¹

$$D_i = D_{i,0} \exp\left(\frac{-E_D}{RT}\right) \quad (3.13)$$

$$K_i^G = K_{i,0}^G \exp\left(\frac{-\Delta H_S}{RT}\right) \quad (3.14)$$

where $D_{i,0}$ and $K_{i,0}^G$ are preexponential factors, E_D is the activation energy of diffusion, and ΔH_S is the enthalpy of dissolution of the permeant in the membrane. Substitution of eqs 3.13 and 3.14 into eq 2.6 gives

$$\overline{P}_i = \frac{D_{i,0} K_{i,0}^G}{\ell} \exp\left(\frac{-(E_D + \Delta H_S)}{RT}\right) = \overline{P}_{i,0} \exp\left(\frac{-E_P}{RT}\right) \quad (3.15)$$

where $\overline{P}_{i,0}$ is the preexponential factor for permeance and E_P is the activation energy for permeability characterizing the combined temperature dependence of sorption and diffusivity. Because temperature affects both the driving force (vapor pressure difference) and the permeance, the thermal dependence of the permeance should be evaluated independently. Substitution of eq 3.15 into eq 2.10 gives

$$\frac{J_i}{p_{i,0} - p_{i,\ell}} = \overline{P}_{i,0} \exp\left(\frac{-E_P}{RT}\right) \quad (3.16)$$

The parameters $\overline{P}_{i,0}$ and E_P can then be determined by taking the natural log of each side and plotting $\ln(J_i/\Delta p)$ vs. T^{-1} where $\ln \overline{P}_{i,0}$ will be the y-intercept and E_P will be the negative of the slope (after multiplying by R) of a linear regression of the data points.⁶¹

This process was performed for all the membranes at the four levels of laser power. The resulting plots (not shown) were linear with R^2 values of 0.92, 0.94, 0.99, and 0.93 for the 0.0, 0.1, 0.4, and 0.6% membranes, respectively. The permeation activation energy, E_p , was exothermic for all membranes and the magnitude of energy release increased linearly according to Au content. Values varied from $-22.7 \text{ kJ mol}^{-1}$ for the 0.0% membrane to -5.7 kJ mol^{-1} for the 0.6% AuNCM. The preexponential factor, $\overline{P}_{i,0}$, increased exponentially with Au content from a value of $10^{-7} \text{ kmol m}^{-2} \text{ h}^{-1} \text{ torr}^{-1}$ for the 0.0% membrane to $1.38 \times 10^{-4} \text{ kmol m}^{-2} \text{ h}^{-1} \text{ torr}^{-1}$ for the 0.6% AuNCM. The next section will discuss what these values indicate with regard to membrane performance and structure; section 3.3.3 will discuss how these values are used to predict the flux of the membranes at higher levels of excitation for the economic analysis.

3.3.2 Perspectives on AuNCM Permeance

Calculated values of permeance decreased with increasing temperature for all the membranes, regardless of Au content (Figure 2.9). As discussed above, E_p is the sum of the activation energy of diffusion, E_D , and the enthalpy of solution, ΔH_S . Typically, the solution process is exothermic and ΔH_S has a value less than zero. When the negative value of ΔH_S dominates over the positive E_D , the permeance of a material will decrease with increasing temperature.⁶¹ It appears this is the case with the AuNCMs. As the Au content of the membranes is increased, however, the negative effect of increasing temperature on the permeance of butanol is partially mitigated. This effect is demonstrated mathematically by the (linearly) decreasing exothermic release of E_p as a function of total Au content. The smaller magnitudes of E_p with increasing Au content mean that the butanol solubility in the membrane is not reduced as much with increasing temperature. Thus, the rate of butanol sorption will be relatively higher in membranes with higher Au content at equivalent elevated temperatures.

The increased sorption rate of the more highly Au concentrated membranes most likely occurs due to increased membrane swelling, defined as the weight fraction of penetrant (butanol) inside the membrane relative to the weight fraction of the dry membrane material.⁸⁰ Additional penetrant in the membrane corresponds to increased mobility of the polymer chains and thus significantly easier permeation through the membrane⁸¹ since diffusivities can increase orders of magnitude as a result of swelling.⁸⁰ A polymer's susceptibility to swelling is directly tied to its elastic modulus. As the modulus is increased (more rigid polymer), the degree to which the membrane will swell under the same conditions is decreased.^{82, 83} In the AuNCMs, introduction of the AuNPs results in two competing effects on the modulus of the composite polymer: i) an increase due to the inclusion of nanoscale particles and ii) a decrease due to the consumption of available crosslinker.

Inclusion of inorganic fillers (e.g., carbon nanotubes) has been shown to substantially increase the mechanical properties of PDMS.⁸⁴ Recently, this effect has been demonstrated with *in situ* reduction of metal salts (silver and gold) in PDMS to form nanocomposites like those examined here.^{85, 86} The nanoparticles were shown to interface well with the PDMS matrix and served to improve mechanical load transfer within the nanocomposite, resulting in a higher modulus.⁸⁶ Formation of the AuNPs in the AuNCMs then can reasonably be expected to increase the elastic modulus to a certain extent and, consequently, prevent swelling. However, the elastic modulus of PDMS decreases strongly as the degree of crosslinking is reduced^{82, 83, 87} because of the increased mobility of the polymer chains.²² Deuschle *et al.* and Stafie *et al.* demonstrated experimentally that PDMS swelling increases significantly in organic solutions when the available crosslinker is reduced.^{82, 83}

As discussed above, it was evident from experimental observations that the AuNCMs were not curing as well when Au content was continually increased, indicating a possible reduction in the degree of crosslinking that resulted from consumption of active crosslinker sites by the ionic Au. The performance of the AuNCMs in this study suggests that the reduction in the membranes' elastic modulus due to reduced crosslinking dominates relative to any increase resulting from inclusion of the AuNPs. Thus, it appears that the diminished decrease in permeance as a function of increasing temperature stems from increased swelling in the highly Au concentrated, but poorly crosslinked, AuNCMs. It should be noted that repeated swelling cycles could detrimentally affect the AuNP/polymer interface, leading to poorer thermal contact or nanoscale defects in the polymer structure. No measurable effects of this type were observed in this study, but attention should be given to this possibility in future work.

3.3.3 Flux Prediction

Within the range of experimental observation, E_p and $\overline{P_{i,0}}$ demonstrated linear and exponential dependence, respectively, on the total Au content of the membrane – as mentioned in section 3.3.1. These relationships enable functions to be defined that predict their values based on Au mass %:

$$E_p = A_1(Au\%) + A_2 \quad (3.17)$$

$$\overline{P_{i,0}} = B_1 \exp[B_2(Au\%)] \quad (3.18)$$

where A_1 , A_2 , B_1 , and B_2 are fitting constants defined by the linear ($R^2=0.81$) and exponential ($R^2=0.83$) regressions. Eq 3.17 and 3.18 can then be substituted into eq 3.16 to give a single empirical relation for flux based on Au mass %, temperature (saturation vapor pressure), and permeate pressure. The results of the relation, as well as the experimentally measured fluxes, are

shown in 3.3.3. The simulated fluxes exhibit excellent agreement with the 0.4% and 0.6% AuNCMs with a maximum error <3%. Agreement is worse for the 0.0% and 0.1% membranes due to the difference in the 0.1% permeance at 0 mW discussed in section 2.3.4. However, the error for all data points is <8% with one exception (9.6%). Flux values do not vary widely at low temperatures and the simulations fall closely together. As temperature is raised, divergence among the fluxes at similar temperatures grows large and the relative accuracy of the empirical relation increases.

3.4 COUPLED MODEL FOR ECONOMIC ANALYSIS

The empirical relation for flux and the thermal model (eq 3.10) were coupled together by setting

$$\dot{m} = J_i A_m MW_i \quad (3.19)$$

where A_m is the active area of the membrane, MW_i is the molecular weight of i , and J_i is the flux of i according to eqs 3.16, 3.17, and 3.18. This coupling created a single model that estimated membrane SS ΔT , flux, and energy efficiencies with only three input parameters: incident laser power, absorbance fraction, and membrane Au content. Using this model, realization of the economic impact prediction given in section 1.4 could be estimated.

The predicted impact was based on experimental data¹⁹ and involved raising the feed temperature from 37 °C to 70 °C for pervaporation, resulting in flux increase by a factor of 4.9. Selectivity was shown not to vary significantly with temperature, so a constant selectivity of 45 was assumed. For the model predictions, all the same conditions were assumed. For each simulation, laser power was raised to achieve a starting temperature of 37 °C (feed temperature) to establish a baseline flux, and it was then adjusted to achieve the flux enhancement factor of 4.9. The resulting energy usage percentages were recorded and input into the economic model.

Thus for simulated plasmonic pervaporation, the utility usage included: i) energy (electricity) needed for permeate vaporization divided by the efficiency predicted by the coupled thermal model and ii) the cooling water (equal on an energy basis) to remove the percentage of heat lost to the feed.

The results are shown in Figure 3.7. Like the results given in Figure 3.5, this analysis was performed both assuming (Figure 3.7 (a)) 100% absorption by of laser light by the membranes (laser power = power absorbed) and (Figure 3.7 (b)) assuming the actual, calculated membrane laser absorbance (taken, for each membrane, as the average of the three values in Figure 3.4). Lines in the figure show the original predictions from Figure 1.2. The shaded regions outline the results calculated from the coupled thermal model – the top and bottom of each region correspond to the 0.6% and 0.0% membranes, respectively. Energy and operating cost reduction are indicated by the blue and red shaded regions, respectively. Areas of the shaded region that fall below the dotted line at a reduction factor of one require more energy or utility cost than the conventional method of feed heating. The model shows that, if the membranes absorbed 100% of the incident laser light (laser power = Q_I in eq 3.10) energy usage and utility cost of the process could be reduced by maximum factors of 6.42 and 2.73, respectively, with the 0.6% membrane. Although, when the calculated absorbance is used, these figures fall to 0.91 and 0.39 for the energy usage and utility cost, respectively, indicating that plasmonic pervaporation will require slightly more energy and cost more than double to operate.

As was previously discussed, the two main losses of energy efficiency in this process are heat loss to the feed and low light absorption in the membranes. The latter is ignored in Figure 3.7 (a) and it can be seen that the control of energy losses to the feed (and other mechanisms) offers ~2-fold enhancement of the economic impact. However, increasing membrane absorbance

has the potential to increase the economic impact of the process by 7-fold (bringing it to the levels shown in Figure 3.7 (a)). Thus, significantly more potential for improvement exists in optimizing the AuNCMs to achieve as much absorption as possible. In the next chapter, a novel spectroscopic approach is used as a first estimate of the physical characteristics of the AuNCMs to investigate why they do not absorb as much light as was expected.

3.5 CONCLUSIONS

The work outlined in this chapter attempted to simulate and understand the experimentally observed plasmonic pervaporation results. A thermal model was proposed to describe the transfer of thermal energy in the plasmonic pervaporation process by a variety of heat transfer modes. Loss of heat to the feed by conduction was shown to align well with an infinite fin model for cooling. The model enabled the absorption fractions of each membrane to be calculated and the resulting values were much smaller than the extinction values given in Chapter 2. An activation energy analysis of the experimental flux data provided an empirical model for predicting membrane permeance as a function of Au content. The mitigated negative thermal dependence of membrane permeance with increased Au content was attributed to increased swelling resulting from overconsumption of crosslinker. The two models were coupled to identify the energy and utility cost savings that were possible with the plasmonic pervaporation process. The process required more energy and was more costly due mainly to low absorption but offered a potential 7-fold enhancement in energy and cost efficiency with improved membrane fabrication. Additional improvements (2-fold) were shown to be possible through reduction of energy loss to the feed.

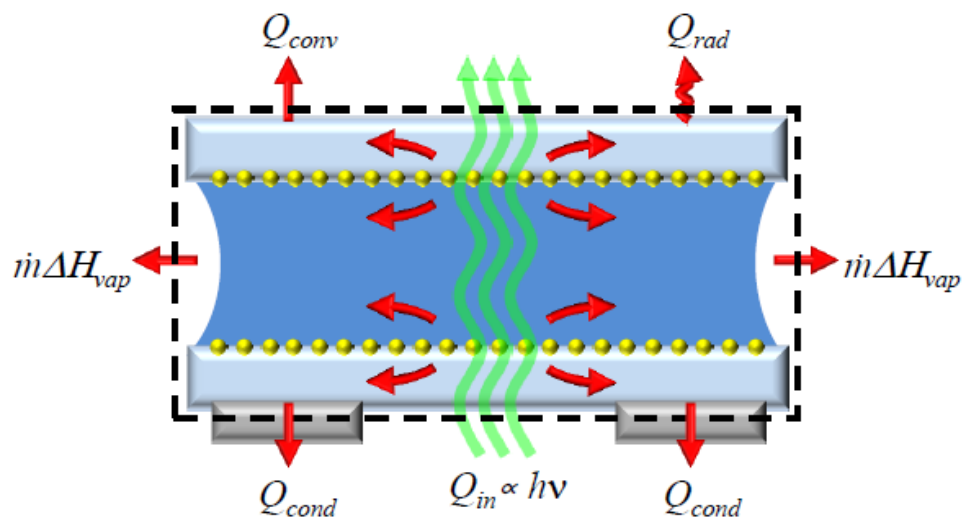


Figure 3.1. Diagram of heat transfer in an open, silica capillary plated with AuNPs.

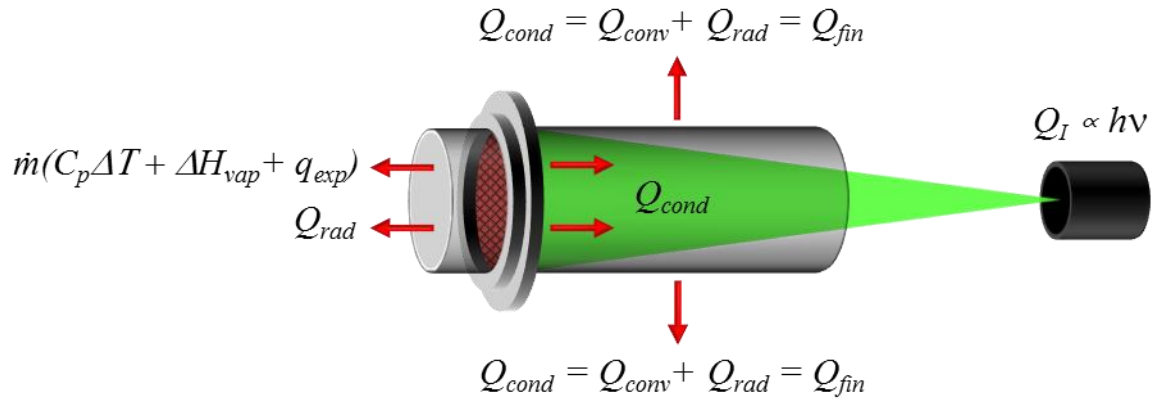


Figure 3.2. Schematic of heat transfer from the laser heated AuNCM in the plasmonic pervaporation system.

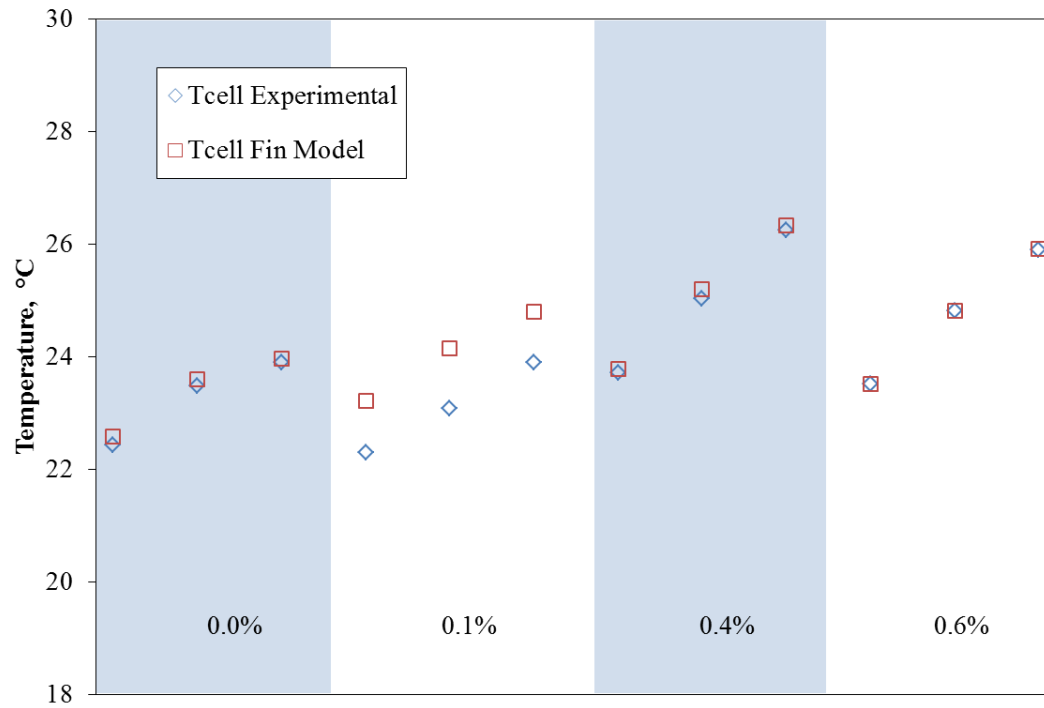


Figure 3.3. Comparison of feed cell temperatures measured experimentally and calculated using infinite fin model for each membrane at 250, 500, and 750 mW laser irradiation (left to right).

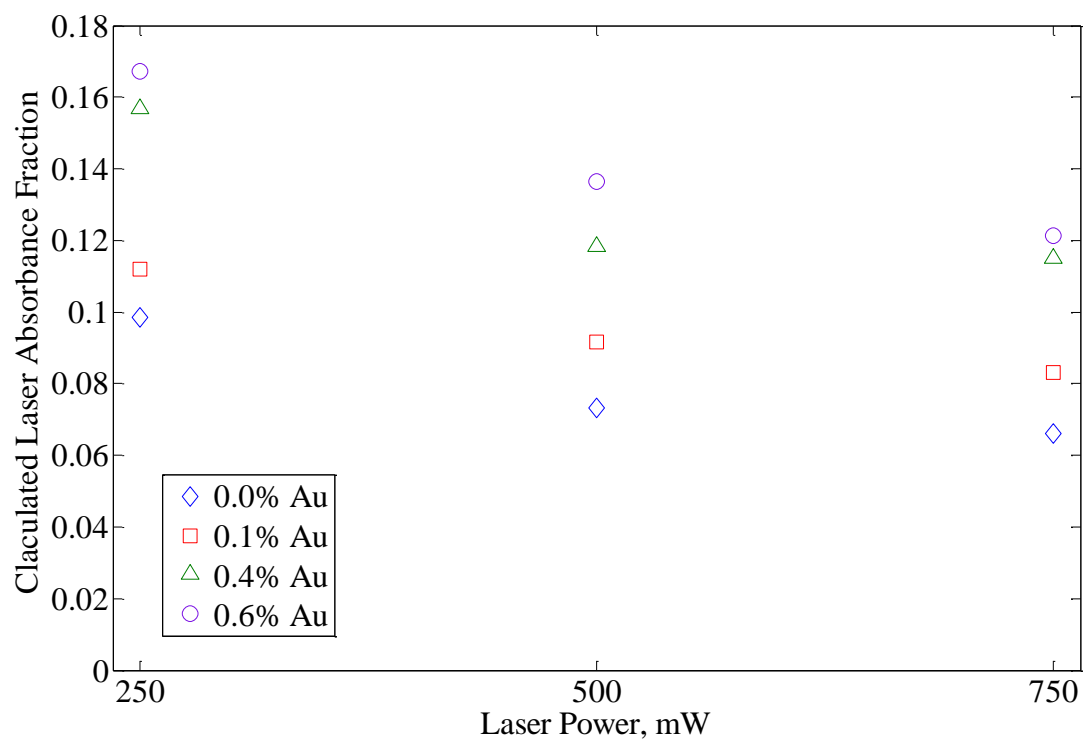


Figure 3.4. Membrane assembly (membrane and stainless steel mesh) laser absorbance fractions for the four membranes at three levels of incident laser power. Representation of the cumulative uncertainty inherent to these values is not shown here, but is discussed at length in Chapter 3.

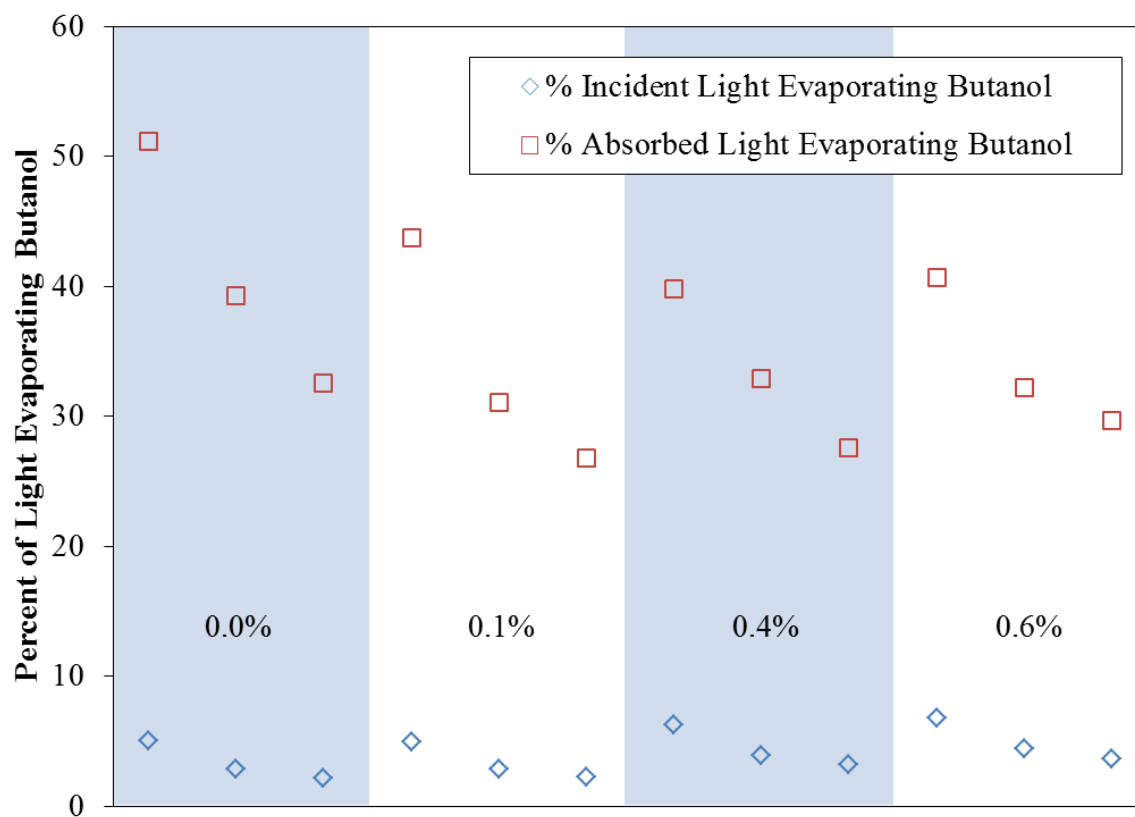


Figure 3.5. Energy consumed by vaporization of butanol permeate on two different bases: i) as a percentage of the incident light and ii) as a percentage of the absorbed light (incident light multiplied by the absorbance fractions in Figure 3.4) at 250, 500, and 750 mW laser irradiation (left to right).

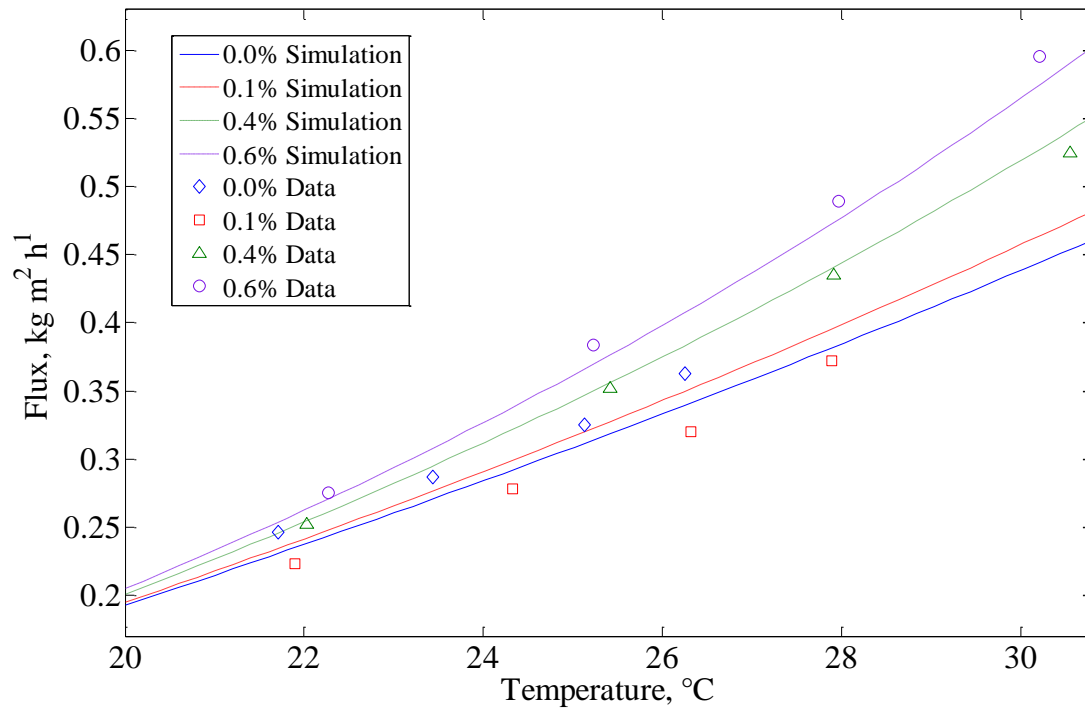


Figure 3.6. Comparison of experimentally measured fluxes and simulated fluxes generated by an empirical model for membrane permeance based on Au content.

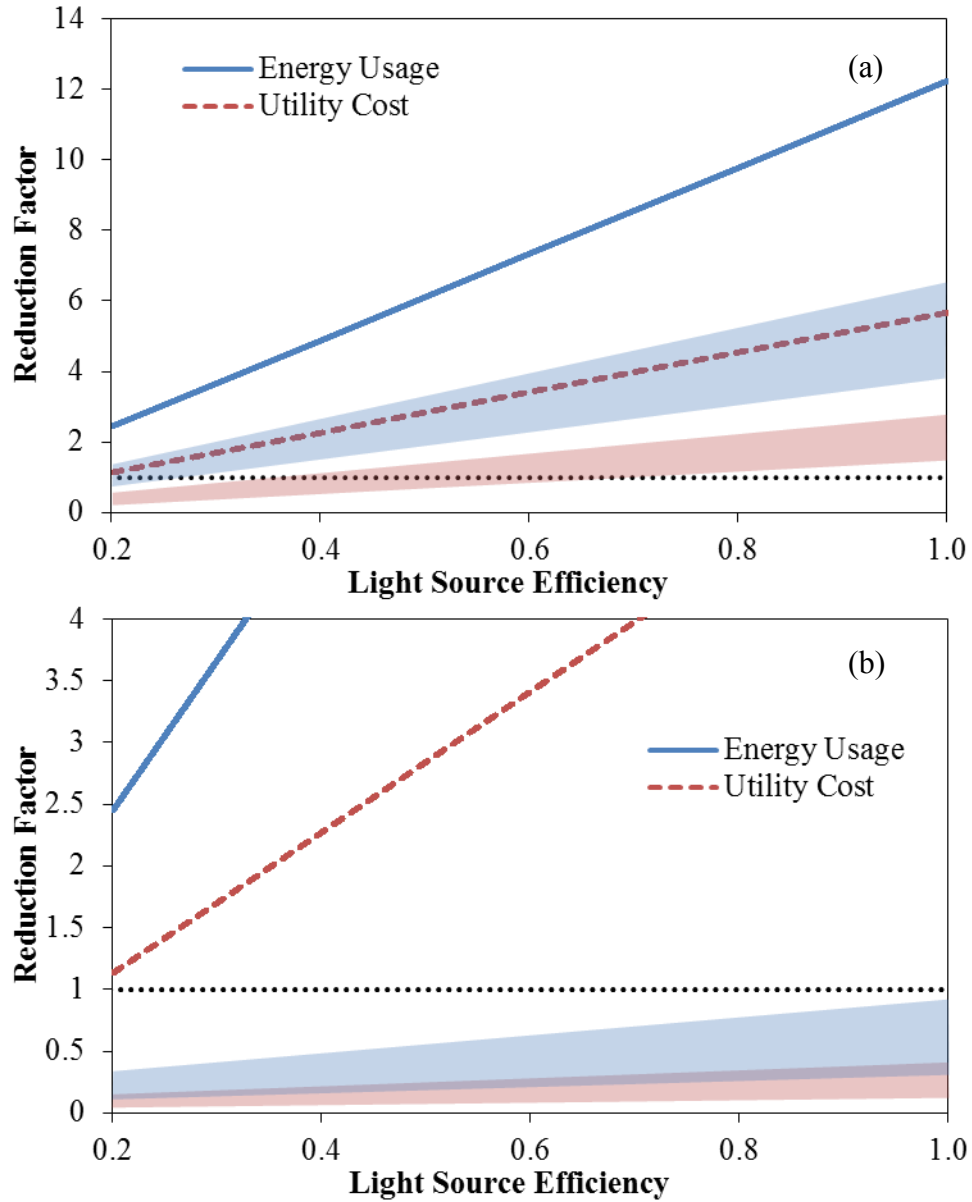


Figure 3.7. Realization (shaded regions) of predicted reduction in energy demand (blue) and utility cost (red) from experimental plasmonic pervaporation results and modeling. Lines show original ideal case (Figure 1.2), shaded regions outline predicted realization according to Au content (top = 0.6% Au, bottom = 0.0% Au) based on (a) absorbed light and (b) incident light.

Table 3.1. Thermoplasmonic model results for each pervaporation data set. All values are in units of mW.

Membrane	Incident Laser Power	Q_I	Q_{fin}	$\dot{m}\Delta H_{vap}$	Q_{rad}	$\dot{m}C_p\Delta T$	$\dot{m}q_{exp}$
0.0% Au	250	24.65	9.35	9.77	2.69	0.07	2.78
	500	36.60	17.44	11.08	4.78	0.13	3.17
	750	49.65	26.48	12.39	7.01	0.22	3.55
0.1% Au	250	28.03	12.30	9.47	3.47	0.08	2.70
	500	45.85	24.96	10.92	6.66	0.18	3.13
	750	62.25	36.19	12.72	9.39	0.29	3.66
0.4% Au	250	39.20	18.54	12.00	5.07	0.15	3.44
	500	59.15	31.41	14.87	8.29	0.30	4.28
	750	86.33	49.81	18.00	12.75	0.56	5.21
0.6% Au	250	41.83	19.52	13.09	5.29	0.17	3.75
	500	68.20	36.75	16.72	9.52	0.39	4.81
	750	90.90	50.95	20.43	12.96	0.65	5.91

CHAPTER 4

INITIAL CHARACTERIZATION OF NANOCOMPOSITE MEMBRANES

4.1 SIGNIFICANCE OF THE PRESENT WORK

In the previous chapters it was shown that plasmonic heating of AuNP-functionalized pervaporation membranes can significantly and stably enhance the flux of butanol; yet, for the system studied, the low levels of light absorption by the membranes reduces the economic impact of the process beyond feasibility. In this chapter, physical properties of the AuNCMs (e.g., AuNP size, concentration, etc.) are investigated to ascertain the cause of the low absorption and identify potential for improvements. It is estimated that only a small fraction (<25%) of the added Au is being reduced to the desired, green light-absorbing AuNPs. Evidence is then provided to suggest that this result may stem from the formation of much larger Au particles that are not plasmon-active at the desired wavelength, but increase the overall light scattering in the polymer matrix, reducing the absorption efficiency.

Several methods of analysis were attempted to determine the physical properties of the AuNCMs. Scanning electron microscopy (SEM, Philips XL40) was performed on the surfaces of the membranes at 5 keV using the backscattering electron detector. Qualitative evidence of the presence of AuNPs (30-80 nm) on the order of the desired diameter was obtained, but charging due to the non-conducting PDMS and the fact that the vast majority of particles were within the polymer matrix, rather than on the surface, prevented accurate evaluation of AuNP

properties. Silver paint was used on the samples to mitigate charging, but was not found to be effective. X-ray photoelectron spectroscopy was performed in unscanned mode (150 eV) on the cross-section of the most concentrated AuNCM (0.6%), but no peak for Au appeared in the spectra. This could have resulted from diffuse AuNP dispersal as well as possible particle removal as the sample was cleaved.

Additionally, attempts were made to remove the AuNPs from the matrix for SEM analysis by dissolving the polymer in sulfuric acid and depositing the solution onto a silica substrate. Multiple lower acid concentrations were tried, but only undiluted (95-98%) acid was capable of dissolving the PDMS. Following dissolution of the polymer, the particles were centrifuged and resuspended in water. A drop of the solution was dried on a glass slide and examined in the SEM. The particles observed in the SEM were typically much larger than expected based on plasmonic response suggesting aggregation had occurred during the removal/deposition process due to the lack of a stabilizing agent. Also, many particles were contained in what appeared to be large agglomerations of polymer. These results prevented accurate analysis of AuNP properties using this approach.

Other investigations of nanocomposite materials such as those examined here have relied upon transmission electron microscopy^{54, 86, 88, 89} (TEM) and, in some cases, X-ray diffraction⁸⁹ for quantitative analysis of AuNP size and, to the author's knowledge, have not attempted to analyze final AuNP concentration in the polymer matrix. TEM analysis is not sufficient to describe the large-scale (15 mm diameter) AuNCMs used here because it is both destructive to the samples and only reasonably capable of investigating extremely small areas within the nanocomposite – on the order of tens to hundreds of square microns. In contrast, UV-vis spectral analysis of the AuNCMs offers the benefits of both not harming the material and investigating

the entire active area. Some researchers have claimed that spectral techniques are only sufficient for qualitative analysis of similar materials (i.e., indication of the presence of NPs),⁹⁰ but it has been well established that UV-vis spectroscopy in conjunction with Mie theory and Beer-Lambert's law can be used to accurately evaluate both average AuNP size and concentration in liquid AuNP composites.^{91, 92} The discussion that follows is an adaptation and extension of these spectral techniques to the solid-state nanocomposites fabricated in this study.

The use of spectroscopic methods to quantify properties of materials of this type is unprecedented, and the methods carry several convoluting factors that could affect the accuracy of the approach. A list of underlying assumptions and potential limitations follows:

1. Defining a common baseline for spectral analysis was difficult because the AuNCMs vary in transparency with Au content, so the raw spectra had to be adjusted.
2. Spectral methods (e.g., Beer-Lambert's law) used were adapted from those used for liquid analysis, not solid nanocomposites such as those in this study.
3. Mie theory (used for AuNP diameter and optical cross-sections) was developed for spherical particles, thus the AuNPs are assumed to be spherical.
4. LSPR peak contributions are assumed to come only from AuNPs at the average diameter.

Efforts were made to identify and discuss possible implications of each difficulty, and literature references are provided to support assumptions where possible. In spite of these considerations, this analysis provides important insights into how Au is consumed in the membranes, and how it might be improved

4.2 UV-VIS SPECTROSCOPIC ANALYSIS

4.2.1 Spectral Adjustment

The raw UV-vis spectra of the 12 AuNCMs, taken with a custom spectral system, are shown in Figure 4.1 (a). As is evident from the figure, there appears to be no common baseline between the samples, even though all were taken under the same conditions and with the same reference (blank glass slide). The variation in baseline most likely results from the loss of transparency associated with increased formation of macroscale agglomerates within the nanocomposite (discussed below). Although the shape of the curves is meaningful and can indicate some information (e.g., average AuNP size), inconsistency in the spectral baseline makes quantitative analysis impossible since meaningful absolute extinction values cannot be extracted. However, the laser extinction fractions given in Figure 2.2 provide an absolute measurement of wavelength-specific (532 nm) extinction by the membranes. These *laser extinction fractions* can be converted to *spectral extinction values* at 532 nm by rearrangement of eq 3.2, given by Roper *et al.*,⁷² to

$$A_{\lambda} = \log\left(1 - \frac{Q_{ext}}{I}\right)^{-1} \quad (4.1)$$

where A_{λ} is the spectral extinction, Q_{ext} is the extinguished laser power, and I is the incident laser power. For this calculation, the transduction efficiency, η_T , is neglected because no distinction is made between absorbed and scattered light.

Once these spectral values are obtained, they provide an anchor for baseline (y-axis) adjustment of the raw spectra shown in Figure 4.1 (a) which, in effect, normalizes the spectra by providing a meaningful common baseline. The adjustment was performed by subtracting the raw spectral extinction value at 532 nm from the entire spectrum and then adding back the spectral extinction value converted from laser extinction fraction (using eq 4.1) in the same way. The

adjusted spectra are given in Figure 4.1 (b). The resulting agreement of spectra for AuNCMs with the same Au content indicates that this normalization is an effective method for baseline correction of these nanocomposite materials and suggests that the adjusted spectra may be used for estimation of material properties. Some of the adjusted spectra fall below zero at longer wavelengths because bare PDMS was not included in the spectral reference, but was accounted for in the laser extinction fraction measurements. The adjusted spectra only show extinction due to the presence of the particles.

4.2.2 Spectral Results

The spectra show impressive similarity in peak location, breadth, and amplitude among the AuNCMs from different batches at the same Au content, providing additional evidence of the reproducibility that is possible with this method. Figure 4.2 (a) shows the LSPR peak locations for each membrane. The LSPR location seems to increase linearly with increasing Au content, with 0.6% occurring as the only exception. On average there is a rise in the LSPR wavelength of 16.4 nm/Au%. The peak locations at equivalent Au content are very closely grouped with the exception of singular outliers for the 0.1% and 0.6% groups. The standard deviation for the 0.4% and 0.75% groups are less than 1 nm (0.7 nm for both). Even with consideration of the outlying points, the standard deviations for the 0.1% and 0.6% groups are quite small at 2.0 nm and 3.3 nm, respectively. The largest divergences among spectral characteristics of the AuNCMs occur at wavelengths much larger than the LSPR wavelength, likely due to differences in the size and concentration of larger, aggregate particles.

If the AuNPs are assumed to be spherical in shape (supported by TEM analysis by others⁸⁶), Mie theory can be used in conjunction with the LSPR locations to determine the average diameter of the AuNPs.⁹¹ For this analysis, the refractive index of the polymer

nanocomposite was assumed to be that of the polymer itself (1.43). Previous studies have shown that inclusion of certain inorganic filler particles in polymer matrices can either significantly raise (e.g., PbS particles) or lower (AuNPs) the refractive index. However, these changes resulted at 10- to 100-fold greater particle concentrations.⁹³ Simulations were run for the LSPR locations given in Figure 4.2 (a) and the resulting averages AuNP diameters are given Figure 4.2 (b). Since the diameter is only dependent on the refractive index (constant) and the LSPR location, the simulated AuNP diameters follow the same trend. There is an average increase in diameter with increasing Au content (~30 nm/Au%) and good agreement among diameters at the same concentration. The 0.4% and 0.75% samples have a very small standard deviation (1.3 nm for both) and the 0.1% and 0.6% AuNCMs have somewhat larger standard deviations (5.1 nm and 7.0 nm, respectively) due to the outlying points.

In addition to particle diameter, Mie theory can be used to calculate, on a spectral basis, the fraction of extinguished light that is absorbed (transduced to thermal energy) rather than scattered by evaluating the ratio of absorption coefficient to extinction coefficient, C_{abs}/C_{ext} . This ratio can be used with the measured overall laser power extinction fraction values shown in Figure 2.2 (Q_{ext}/I from eq 4.1) and further manipulation of eq 3.2 to directly calculate the transduction efficiency for each AuNCM:

$$\eta_T = \frac{Q_{abs}}{Q_{ext}} = \frac{Q_{abs}/I}{Q_{ext}/I} = \frac{1 - 10^{-[(C_{abs}/C_{ext})A_\lambda]}}{Q_{ext}/I} \quad (4.2)$$

where η_T is the transduction efficiency defined as the ratio of absorbed (consumed) laser power, Q_{abs} , to total extinguished laser power, Q_{ext} . This value should be as high as possible as scattered laser light results in a net energy loss in the plasmonic pervaporation process. Figure 4.3 shows the fraction of incident laser light that is predicted to be absorbed by the particles, $(Q_{ext}/I)\eta_T$.

An important result of this analysis is that the absorption fraction of the 0.6% Au membrane is <5% smaller than that of the 0.75% (0.52 vs. 0.54, respectively) even though the overall extinction fraction at 0.75% was 14.1% higher. This difference results from the samples' relative average diameter and the fact that the ratio, C_{abs}/C_{ext} , decreases rapidly as AuNP size increases. The 0.75% samples have an average diameter of 545 nm with an average transduction efficiency of 0.88 compared to 533 nm and 0.96 for the 0.6% sample. It appears that Au content of 0.75% represents not only a curability limit (discussed above), but also may act as an absorption limit due to increasing AuNP diameter. These results suggest that 50-55% laser absorption is the maximum light-to-heat conversion efficiency achievable by AuNCMs of this thickness without altering the fabrication method. Possible means of improving this efficiency are discussed later.

The absorption values in Figure 4.3 should correspond (though not agree due to convolution by the steel mesh) to the absorption efficiencies (Figure 3.4) calculated in the previous chapter. The average (over the three laser powers) calculated absorption efficiencies for the 0.1, 0.4, and 0.6% AuNCMs were 0.096, 0.130, and 0.142 compared to values from the spectral analysis of 0.075, 0.376, and 0.520, respectively. There is close agreement for the 0.1% AuNCM (not accounting for absorption by the mesh), but differences increase substantially with increasing Au content. The reason for the increasing disparity between values estimated from the two methods is most likely an increase in the formation of large, scattering particles in the polymer matrix. This conclusion, with supporting evidence, will be discussed below.

4.3 ESTIMATION OF AuNP CONCENTRATION

Beer-Lambert's law enables the calculation of the concentration of an absorbing element in a solution using spectral analysis. It is given as $A_\lambda = \varepsilon_\lambda \ell c$, where A is spectral extinction, ε is

the wavelength-dependent molar extinction coefficient of the absorbing element, ℓ is the path length of light through the sample (membrane thickness), and c is the molar concentration. It was demonstrated by Liu *et al.* that this relation could be used to accurately determine the concentration of AuNPs in solution. Furthermore, they developed a double logarithmic relation for calculation of the molar extinction coefficient of AuNPs in solution as a function of particle diameter. The relation was given as

$$\ln \varepsilon_{\lambda} = k_p \ln D + a_p \quad (4.3)$$

where k_p and a_p are experimentally-determined constants and D is the particle diameter. The relation is specific to a wavelength of 506 nm and was shown to be independent of solution and capping ligand (i.e., refractive index-independent).⁹⁴ The adjusted spectra in Figure 4.1 (b) can be combined with Beer-Lambert's law and eq 4.3 to estimate AuNP concentration (NP mL⁻¹) in the AuNCMs using the following equation:

$$c_{AuNP} = \frac{A_{506} N_A}{10^3 \exp(k_p \ln D + a_p) \ell} \quad (4.4)$$

where c_{AuNP} is the AuNP concentration in NP mL⁻¹, A_{506} is the extinction at 506 nm taken from the adjusted spectra, N_A is Avogadro's number, 10^3 is a conversion factor from L to mL, and ℓ is the thickness of each AuNCM (74-79 μ m). There are three important assumptions inherent to this calculation: i) Beer-Lambert's law holds true for solid-state nanocomposite materials,⁸⁸ ii) the laser extinction-adjusted spectral extinction values are accurate, and iii) all extinction at 506 nm is directly attributable to AuNPs at the average diameter of each AuNCM.

The calculated AuNP concentrations are given for each membrane in Figure 4.4 (a). The resulting AuNP concentrations are remarkably consistent within each sample set. The largest variation occurs in the 0.6% set, although the respective concentrations are well within the same

order of magnitude, varying by <4-fold. The divergence in the concentrations of the two outlying points results from their smaller average diameters compared to the remaining point in the set. As a percentage of the average concentration, the standard deviation of the 0.1% set is slightly less than that of the 0.6% set – 50.0% and 52.5%, respectively. Relative concentrations in the 0.4% and 0.75% sample sets are significantly more closely aligned with standard deviations of 14.4% and 5.7% of the average concentration, respectively. This level of consistency is impressive given the facile methods used to produce the AuNCMs.

4.3.1 Insights into AuNP Growth

Interestingly, excluding the two outlying points at 0.6%, there is excellent agreement among the AuNP concentrations across sample sets at different levels of Au content, with a maximum difference of only 5-fold between the smallest and largest concentrations. Growth of AuNPs in solution is widely described as involving two steps: i) particle nucleation involving the coalescence of Au atoms into small nuclei and ii) particle growth involving both addition of Au atoms to existing nuclei and the coalescence of small particles.^{92, 95, 96} Further investigation of AuNCM fabrication would be required to draw firm conclusions regarding the exact growth mechanism involved, but analysis of the data in Figure 4.4 (a) provides an initial perspective. The consistency among different levels of Au content suggests that the AuNP growth mechanism followed in all the AuNCMs is similar, regardless of the total Au content (over the range of examined concentrations). In other words, a comparable number of nucleation sites appear to form in each membrane and any additional Au content is primarily funneled toward growth of existing particles rather than formation of additional nucleation sites. This conclusion is further evidenced by the general upward trend of AuNP diameter as Au content is increased.

4.3.2 Gold Utilization

Knowledge of the AuNP concentration and their average diameter enables the approximation of the percentage of added Au that is converted to 532-nm extinguishing AuNPs. This percentage is calculated as

$$C_{\%} = \frac{c_{AuNP} V N_{Au} MW_{Au}}{N_A m_{Au}} \cdot 100\% \quad (4.5)$$

where $C_{\%}$ is the conversion percentage, V is the total solution volume (2.2 mL), N_{Au} is the number of Au atoms per AuNP calculated using the average diameter and the bulk density of Au (19.3 g/mL), MW_{Au} is the molecular weight of Au, and m_{Au} is the total mass of Au added to the solution (2.2-16.5 mg). The conversion percentages for all AuNCMs are given in Figure 4.4 (b). There is again a high level of consistency among the different batches at each level of Au content. The average values of $C_{\%}$ for the 0.1, 0.4, 0.6, and 0.75% samples are 15.6, 22.9, 28.0, and 20.8% with standard deviations of only 2.4, 1.3, 2.9, and 0.9%, respectively. At 0.6%, the agreement of $C_{\%}$ is much stronger than it is for concentration among the three batches, which results from the smaller diameters of the two outlying points from Figure 4.4 (a). $C_{\%}$ does not seem to follow a trend with increasing Au content, but rather, all the values fall within a small window of variation. The average $C_{\%}$ for all twelve AuNCMs is 21.8% with a standard deviation of only 5.0%. This result suggests that, on average for all samples, less than 25% of the added Au is being effectively used for formation of AuNPs that are plasmon-resonant at the excitation wavelength of 532 nm.

This analysis provides several important insights regarding these materials. First, the consistency in conversion percent provides further evidence that the AuNCMs are following a highly similar growth mechanism that is stable across a wide range of Au contents. From a

practical standpoint, it is important that such a small amount of added Au is producing the desired plasmonic AuNPs. This observation suggests that optimization of fabrication methods could produce AuNCMs with significantly higher (≥ 4 -fold) laser absorption capabilities. Lastly, if it is assumed that no Au is left in ionic form, it follows that the majority of the Au content is forming larger, undesirable particles. Evidence and discussion of this conclusion is provided in the following section.

4.4 EVIDENCE OF THE PRESENCE OF LARGE PARTICLES

There are two indications of increasing formation of large particles with increases in total Au content. The first is the consistency of conversion percent for all the AuNCMs. Since a comparable fraction of Au content at each level is being used to form the larger, undesirable particles, the concentration of these particles will increase with total Au content. The second indication of increased large particles is reduced transparency in the membranes. Light scattering in polymer nanocomposites containing random dispersions of primarily small particles (absorbing) occurs at low levels and is virtually absent when compared to similar materials containing equivalent volume fractions of larger particles (scattering). Therefore, composites containing small particles are transparent and, as particle size increases, the composite material will become increasingly opaque. The opacity will also increase as a function of particle aggregation.⁹⁷ Figure 4.5 shows digital images of lines viewed through AuNCMs at each concentration under the same conditions. It is apparent from the figure that the AuNCMs become increasingly opaque – indicating increasing concentration of light-scattering large particles – in addition to becoming deeper in color – indicating increasing concentration of light-absorbing small particles. This could explain why, although 0.6% AuNCMs appear to absorb significantly more light than the 0.4% AuNCMs (Chapter 2), their thermal behavior under

operation is essentially equivalent. To the naked eye, the 0.6% AuNCM appears a deeper reddish color, indicating a higher concentration of plasmonic AuNPs. However, the reduced transparency of the polymer matrix would cause more light scattering, resulting in a proportionally decreasing fraction of light reaching AuNPs located at increasing depths. Thus, a larger concentration of plasmonic AuNPs may not necessarily result in a proportionally higher thermal response under the same level of laser irradiation.

The loss of intensity at a specific wavelength due to the presence of large particles can be estimated using the equation⁹⁸

$$\frac{I_T}{I} = \exp \left\{ - \frac{32\Phi_p \ell \pi^4 r^3 n_m^4}{\lambda^4} \left[\frac{(n_p/n_m)^2 - 1}{(n_p/n_m)^2 + 2} \right]^2 \right\} \quad (4.6)$$

where I_T/I is the transmittance fraction of light at wavelength, λ , Φ_p is the volume fraction of particles in the polymer, ℓ is the thickness of the composite material (membrane thickness), r is the particle radius, n_p is the refractive index of the particles, and n_m is the refractive index of the polymer. Simulations were run using this relation at a wavelength of 532 nm for each concentration of AuNCM assuming particle diameters from 0-700 nm and 0-100% conversion of total Au content to particles of that size (converted to volume fraction for use in eq 4.6). The results for the four concentrations of AuNCMs are shown in Figure 4.6. This relation does not predict plasmonic activity and thus, is only provided for qualitative evidence.

The transmittance fraction falls sharply (increased scattering) both as particle size increases and as a higher percentage of Au is transformed to particles of a particular size. As would be expected, the effects are more extreme at higher Au content. For example, for 0.1% AuNCMs, 80% conversion of Au content to 200 nm particles results in a transmittance fraction

of 0.91 (>90% of light unaffected). The same conditions for the 0.75% AuNCM yield a transmittance fraction of only 0.49. These theoretical results are entirely consistent with the conclusions drawn from the images in Figure 4.5 and the data in Figure 4.4 (b). It was demonstrated a comparable percentage (~78% on average) of added Au was converted to undesirable, large particles for all membranes. Since a larger mass of Au is available to form large particles at higher levels of Au content, the resulting particles will form with larger diameters and/or in higher concentration. Both phenomena induce lower transmittance fractions as was predicted in Figure 4.6 and higher levels of nanocomposite opacity as was experimentally observed in Figure 4.5.

This observation has the potential to reduce the accuracy of the AuNP concentrations given in Figure 4.4 (a). If a high concentration of larger particles is present in the AuNCMs, they could be contributing to the total extinction at 532 nm. The degree to which the accuracy of the concentrations is affected depends on both the size distribution of the large particles and the total Au content of the material. For example, a transmittance fraction of 0.9 at 532 nm is still achieved (meaning a small effect on total extinction at 532 nm) with 78% conversion of the added Au to 205, 127, 113, and 106 nm particles for 0.1, 0.4, 0.6, and 0.75% AuNCMs, respectively. Thus, calculation of concentration most likely decreases in accuracy as Au content increases. This effect could account for the increasing differences between the predicted absorbance values and those calculated from the thermal model. However, the presence of large particles would most likely cause an overestimation of the calculated AuNP concentrations and, by extension, the total conversion percentage of Au to desirable AuNPs. This result would imply an even larger increase in plasmonic activity at 532 nm is possible by further refinement of fabrication methods.

4.5 CONCLUSIONS

This chapter provided a novel spectroscopic method for estimating Au utilization in the AuNCMs. Twelve AuNCMs formed by reduction of TCA in different concentrations were analyzed. AuNCMs made in different batches with equivalent Au content demonstrated highly similar properties indicating a high level of reproducibility in the fabrication method. The spectral analysis was used to estimate AuNP concentration and the percentage of added Au that was converted to 532 nm-resonant AuNPs. The analysis concluded that <25% of Au was converted to desirable AuNPs for all levels of Au content indicating significant (≥ 4 -fold) potential for increased plasmonic response with refinement of fabrication methods. Evidence of large particle formation was provided and evaluated against theoretical predictions. The large particles appear to be the root of poor Au utilization and low laser absorption in the AuNCMs. Preventing large particle formation by optimizing fabrication methods could result in significant increases in AuNCM absorption efficiency. Some suggestions on how this may be achieved are given in the final chapter.

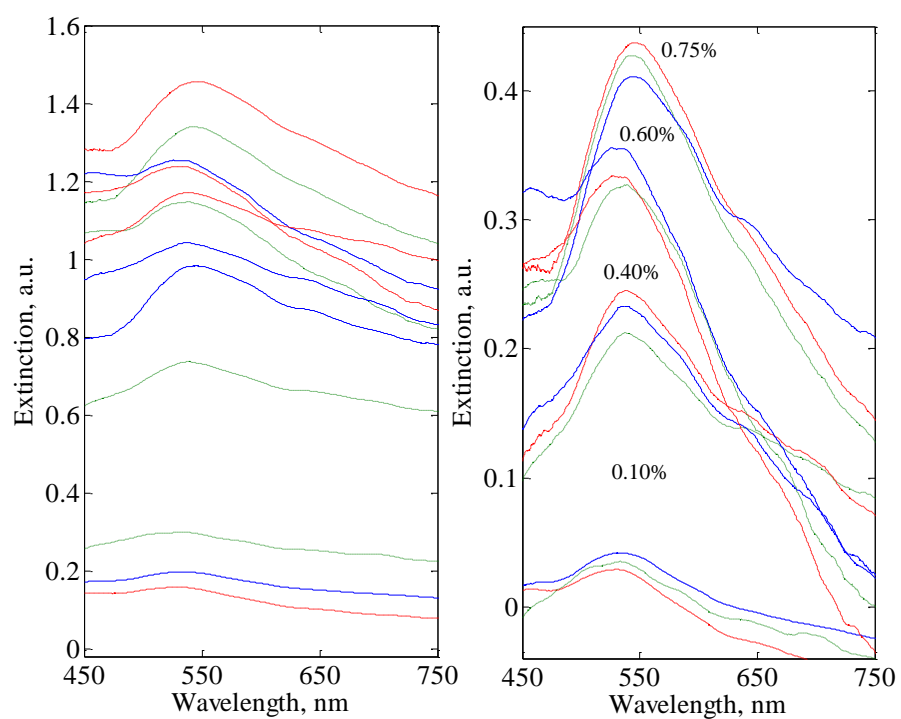


Figure 4.1. Unadjusted (a) and laser extinction adjusted (b) UV-vis spectra of 12 AuNCMs (three batches at the 4 concentrations shown). Solid, dashed, and dotted lines indicate batch 1, 2, and 3, respectively.

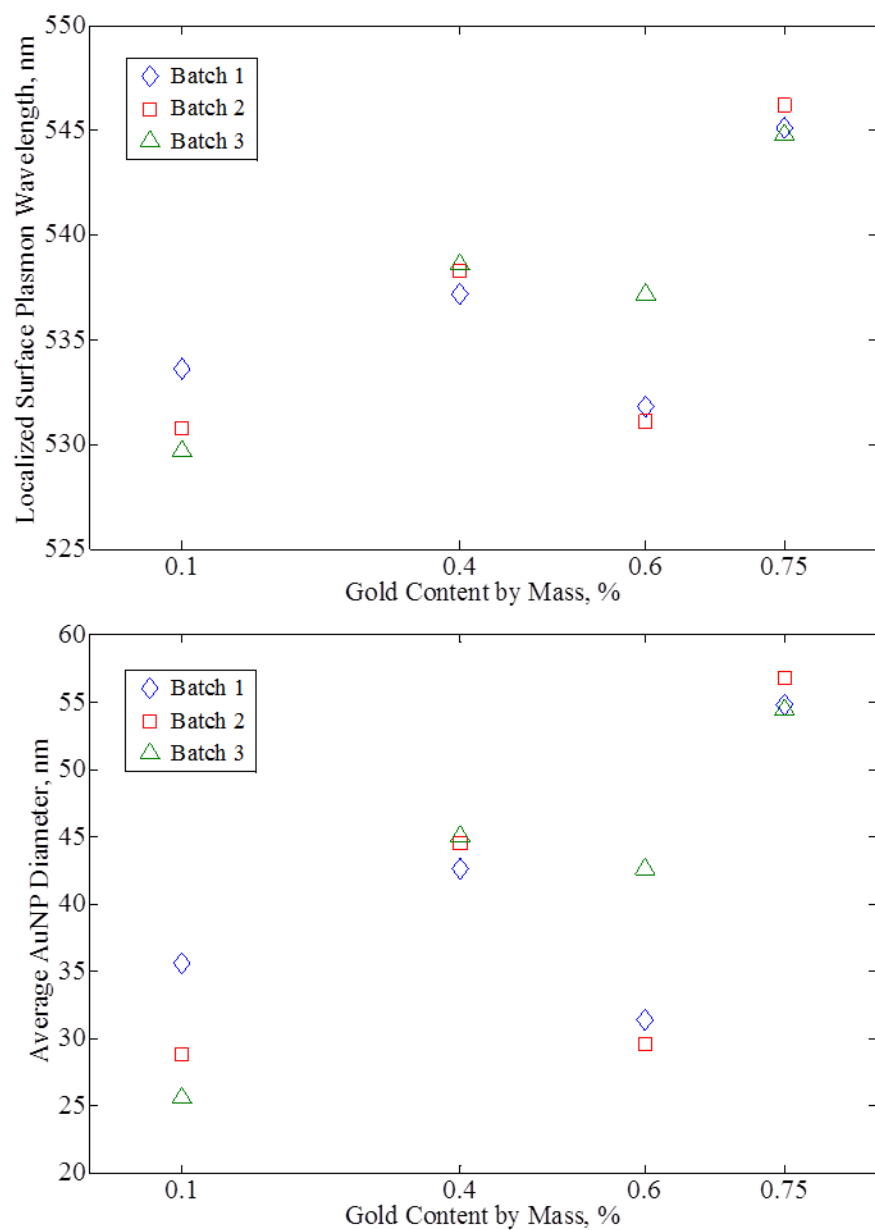


Figure 4.2. Localized surface plasmon wavelength (a) and average AuNP diameter (b) for the 12 AuNCMs (three batches at the 4 concentrations shown).

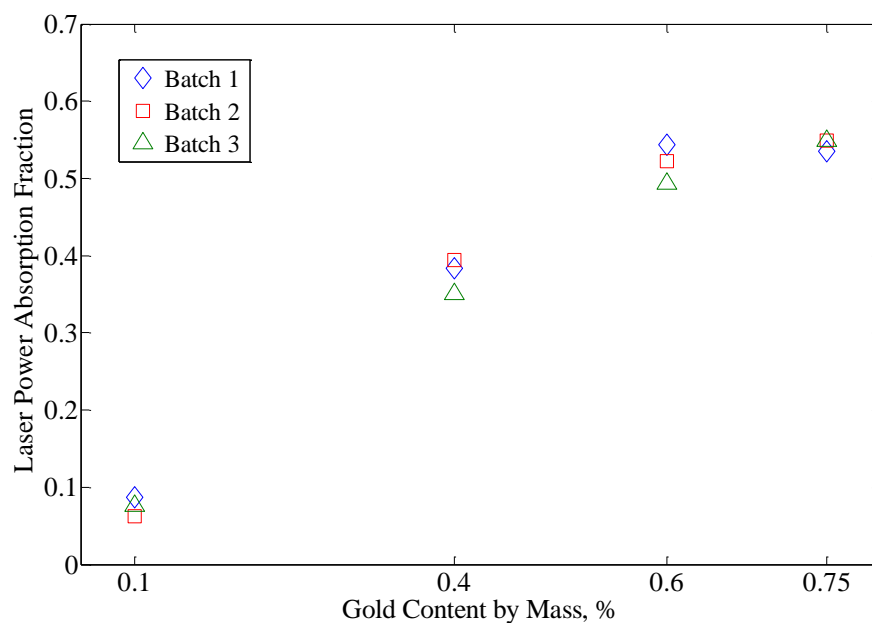


Figure 4.3. Values of estimated laser power consumption (excludes scattered laser light) fraction for Au-NCMs from three different batches at four different values of gold content.

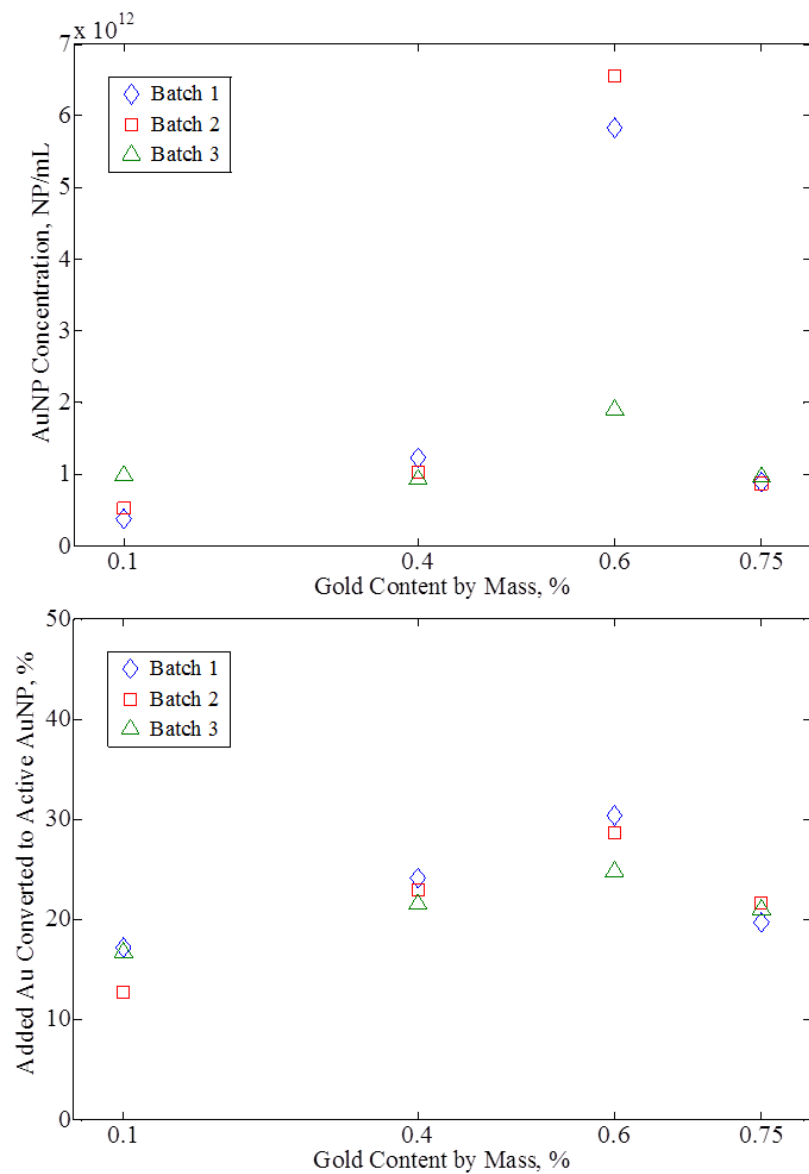


Figure 4.4. Estimated concentration of AuNPs (a) of the average diameters given in Figure 4.2 and percent conversion of added Au to AuNPs of this type (b).

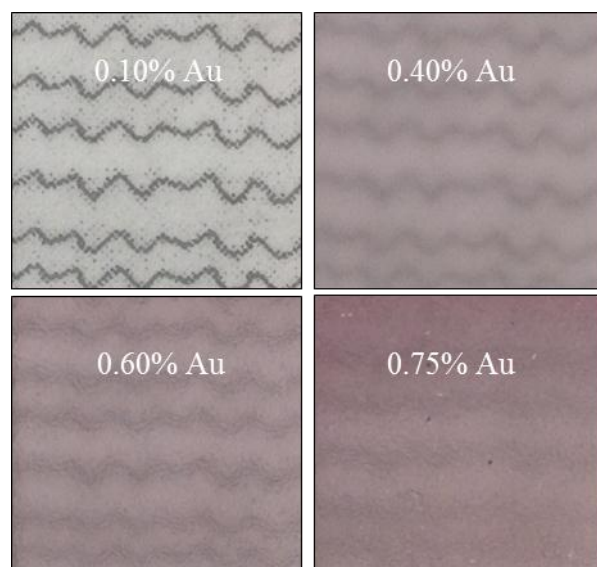


Figure 4.5. Increasing opacity of AuNCMs with increasing Au content indicating increasing concentration of large particles.

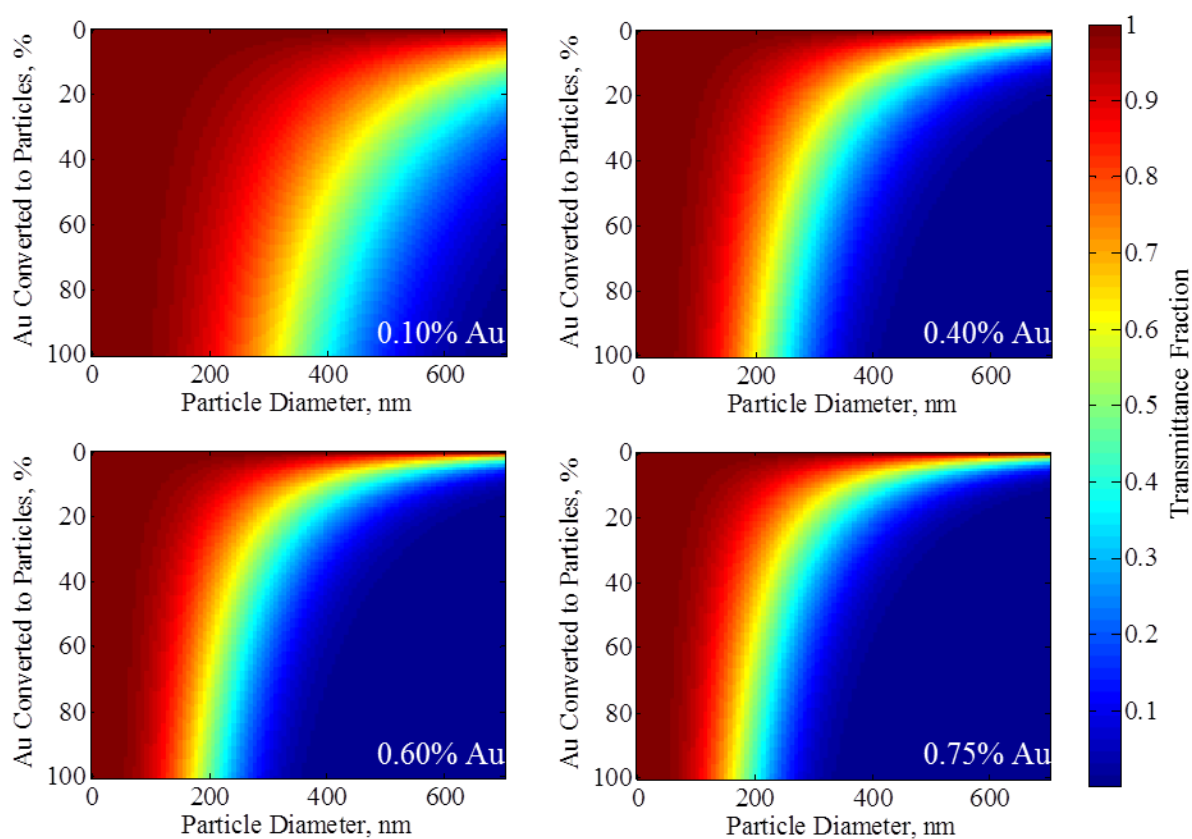


Figure 4.6. Simulations of transmittance fraction of 532 nm light due to particle scattering for four concentrations of AuNCM for particle diameters from 0-700 nm and for 0-100% conversion of total Au content to particles of that size.

CHAPTER 5

CONCLUDING REMARKS

The ability to carefully and precisely introduce thermal energy into a process via plasmonic heating is a powerful tool. The purpose of this project was to demonstrate that plasmonic heating of gold nanoparticle-functionalized, polymer nanocomposite membranes (AuNCMs) in a pervaporation system could increase flux and lower energy demand in the process to reduce the production cost of biobutanol. Experimental investigation showed plasmonic membrane heating effectively increased butanol flux with controlled energy loss to undesired mechanisms (feed heating, etc.). AuNCM absorption efficiencies in the system were too low to achieve the predicted economic impact of the process; however, analysis of the AuNCM physical and optical properties indicated that significant improvements are possible by optimization of fabrication techniques. These improvements have the potential to make plasmonic pervaporation economically superior to conventional methods.

The sections that follow summarize the findings of this study, discuss areas of ongoing work, and suggest future areas of focus.

5.1 SUMMARY OF FINDINGS

5.1.1 Plasmonic Pervaporation System and Performance

Pervaporation flux enhancements of >100% were demonstrated using electromagnetic excitation of AuNCMs. Enhancements were measured in a plasmonic pervaporation system that

was designed and constructed to allow uniform laser excitation and complete thermal analysis of the membrane, as well as automated operation and data capture (flux, membrane and feed temperature, permeate pressure, and ambient conditions). AuNCMs were fabricated in varying concentrations by reduction of tetrachloroauric acid to gold nanoparticles in polydimethylsiloxane facilitated by active sites in the polymer crosslinker. The AuNCMs reached laser extinction percentages of >50% depending on Au content. Stable increases in average membrane temperature (up to ~8 °C) and flux enhancements (up to ~117%) were achieved and increased as a function of both total Au content and incident laser power. Membrane thermal analysis allowed the permeance of each AuNCM to be evaluated as a function of membrane temperature change. The permeance of each membrane fell as a function of temperature change at a rate that decreased with increasing Au content.

5.1.2 Thermal Modeling

A thermal model was developed to calculate the absorption efficiencies of the membrane assemblies in operation and quantify how energy is transferred within the plasmonic pervaporation system. The model treated the membrane and support mesh as a single system with one power input (the laser) and multiple power outputs. Power lost to the feed by conduction was shown to align well with an infinite fin model. Calculated absorption of incident laser light fell well below laser extinction percentages measured outside the system. Thermal analysis of heat transfer mechanisms showed that conduction to the feed was the largest mode of energy loss in the system, accounting for 38% to 58% of total heat loss depending on conditions. The amount of input energy consumed by permeate vaporization varied from 20% to 40% and generally decreased with increasing laser absorption. Other important modes of heat transfer included radiation from the AuNCM/mesh and heat of isothermal expansion of the permeate.

Energy losses to the feed and to radiative transfer should be minimized to increase the efficiency of the process.

5.1.3 Pervaporation Modeling and Economic Analysis

The dependence of membrane permeance on temperature and Au content were characterized using an activation energy analysis of the experimental flux data. The analysis provided the development of an empirical model for predicting membrane permeance. The mitigated negative thermal dependence of membrane permeance with increased Au content was attributed to increased swelling resulting from overconsumption of crosslinker. The empirical model for permeance was coupled with the thermal model to evaluate the energy and utility cost savings that were possible with the plasmonic pervaporation process and how they compared to the initial predictions. The analysis showed plasmonic pervaporation required more energy and was more costly than conventional feed heating due to the low laser absorption in the membranes. However, the analysis showed the potential for 7-fold enhancement in energy and cost efficiency with improved membrane fabrication and up to 2-fold enhancements from reduction of energy loss to the feed.

5.1.4 AuNCM Characterization

Finally, the physical and optical properties of the AuNCMs were estimated using a novel spectroscopic approach to evaluate the reason for the low laser absorption efficiencies. Twelve AuNCMs formed by reduction of TCA in four different concentrations were analyzed. AuNCMs with equivalent Au content demonstrated very similar properties indicating a high level of reproducibility in the fabrication method. The spectral analysis showed that, on average, <25% of added Au was converted to desirable AuNPs for all levels of Au content. This result indicated that ≥ 4 -fold potential exists for increased plasmonic response with refinement of fabrication

methods. Evidence of large particle formation was provided and identified as the most likely reason for the low absorption efficiencies and a possible means of reducing the accuracy of the spectral analysis. The improvement of fabrication methods to reduce large particle formation and increase light absorption was demonstrated to be largest source of potential improvement in the process of plasmonic pervaporation.

5.2 ONGOING AND FUTURE WORK

The sections below discuss work currently being performed as well as suggested research areas to improve upon the current state of plasmonic pervaporation. Some alternative applications are also suggested.

5.2.1 Improvements in Current System

There are several possible system and experimental modifications that were discussed that could reduce uncertainty in the thermal model. First, incorporation of a mechanical membrane support that is optically inert will offer improved negative control experiments and deconvolute determination of the AuNCM efficiencies. A rigid, plastic mesh support may accomplish this goal. Secondly, the measurement of additional thermal points along the length of the feed tube would provide a more direct indication of the thermal profile and the associated heat loss. Also, if radial heat transfer is significant in the membrane, thermal insulation of the membrane assembly may allow a more uniform membrane thermal profile to be established.

5.2.2 Investigation of Selectivity

Plasmonic pervaporation results in this study were for butanol alone, but the effects of AuNP inclusion, crosslinker consumption, and plasmonic heating of the AuNCMs on membrane selectivity will be extremely important. Currently, we are beginning experiments similar to those herein, but with pure water rather than butanol. The relative behavior of the two components

will provide an initial indication of selectivities that may be attained in the plasmonic pervaporation system. Using multiple components simultaneously in the stagnant pervaporation cell would result in dynamically evolving concentration gradients in the feed due to the lack of mixing. Eventually, the cell could be redesigned to allow flow across the membrane from a mixed vessel to enable direct determination of selectivity.

5.2.3 AuNCM Thermal Properties

We have recently characterized the spectral properties and thermal behavior of AuNP-functionalized polymer nanocomposite films fabricated by different methods (TCA reduction and pre-formed AuNP dispersion).⁹⁹ Currently, work is being performed to estimate the transduction efficiencies and thermal conductivities exhibited by these materials.¹⁰⁰ The analysis will examine how these properties change with increasing Au content and with different fabrication methods. The results will provide helpful insights into how the absorption efficiencies of the AuNCMs may be improved.

5.2.4 Membrane Optimization and Characterization

The present work concluded that the greatest potential for improvement in plasmonic pervaporation is in membranes fabrication. The analysis showed hypothetical increases in absorption efficiency of ≥ 4 -fold are possible. The focus should be on reducing the formation of large, light-scattering particles. Some suggested approaches are:

1. *Varying fabrication methods.* This could include different curing temperatures/times, staged TCA addition and mixing, or sonication⁸⁸ during AuNP growth to prevent aggregation and stimulate additional nucleation.
2. *Increasing crosslinker concentration.* It was mentioned previously that AuNCMs did not cure well with $>0.6\%$ Au by mass. It may be possible to increase Au content by providing

a higher fraction of crosslinker. This may also result in higher AuNP concentration from the additional site for possible nucleation.

These improved methods will serve both to increase the economic impact of plasmonic pervaporation and the accuracy of the spectral characterization method developed in this work.

It has also been suggested that alternative particle analysis techniques such as small-angle scattering, energy-dispersive x-ray spectroscopy, and x-ray photoelectron spectroscopy could be employed to estimate AuNCM properties. Collaboration with investigators familiar with application of these techniques to nanoscale analysis could provide direct, *in situ* characterization of particle size distribution, concentration, and interface composition.

5.2.5 Additional Applications

It has been demonstrated herein that the localized introduction of energy can strongly benefit a process in terms of productivity and energy efficiency, but this effect is not limited to pervaporation. This same approach could be applied in alternate membrane separations, catalytic systems, and heating in microfluidic channels.

REFERENCES

1. Qureshi, N.; Ezeji, T. C. Butanol, 'a Superior Biofuel' Production from Agricultural Residues (Renewable Biomass): Recent Progress in Technology. *Biofuels, Bioproducts and Biorefining* **2008**, 2, 319-330.
2. Duerre, P. Biobutanol: An Attractive Biofuel. *Biotechnology Journal* **2007**, 2, 1525-1534.
3. Vane, L. M. A Review of Pervaporation for Product Recovery from Biomass Fermentation Processes. *Journal of Chemical Technology & Biotechnology* **2005**, 80, 603-629.
4. Kraemer, K.; Harwardt, A.; Bronneberg, R.; Marquardt, W. Separation of Butanol from Acetone-Butanol-Ethanol Fermentation by a Hybrid Extraction-Distillation Process. *Computers & Chemical Engineering* **2011**, 35, 949-963.
5. Friedl, A.; Qureshi, N.; Maddox, I. Continuous Acetone-Butanol-Ethanol (ABE) Fermentation using Immobilized Cells of *Clostridium Acetobutylicum* in a Packed Bed Reactor and Integration with Product Removal by Pervaporation. *Biotechnology and Bioengineering* **2004**, 38, 518-527.
6. Kujawski, W. Application of Pervaporation and Vapor Permeation in Environmental Protection. *Polish Journal of Environmental Studies* **2000**, 9, 13-26.
7. Lin, L.; Zhang, Y.; Kong, Y. Recent Advances in Sulfur Removal from Gasoline by Pervaporation. *Fuel* **2009**, 88, 1799-1809.
8. Huh, H.; Rhim, J. W.; Park, J. S.; Nam, S. Y. Petroleum Separation through Polymer Blend Membranes by using Pervaporation. *Materials Science Forum* **2005**, 486-487, 432-435.
9. White, L. S. Development of Large-Scale Applications in Organic Solvent Nanofiltration and Pervaporation for Chemical and Refining Processes. *Journal of Membrane Science* **2006**, 286, 26-35.
10. Shao, P.; Kumar, A. Separation of 1-butanol/2,3-Butanediol using ZSM-5 Zeolite-Filled Polydimethylsiloxane Membranes. *Journal of Membrane Science* **2009**, 339, 143-150.
11. Wang, Y.; Chung, T. S.; Wang, H. Polyamide-Imide Membranes with Surface Immobilized Cyclodextrin for Butanol Isomer Separation Via Pervaporation. *AIChE J.* **2011**, 57, 1470-1484.
12. Choudhari, S. K.; Kariduraganavar, M. Y. Development of Novel Composite Membranes using Quaternized Chitosan and Na⁺-MMT Clay for the Pervaporation Dehydration of Isopropanol. *Journal of Colloid and Interface Science* **2009**, 338, 111-120.

13. Sommer, S.; Melin, T. Design and Optimization of Hybrid Separation Processes for the Dehydration of 2-Propanol and Other Organics. *Industrial & Engineering Chemistry Research* **2004**, *43*, 5248-5259.
14. Zhang, W.; Sun, W.; Yang, J.; Ren, Z. The Study on Pervaporation Behaviors of Dilute Organic Solution through PDMS/PTFE Composite Membrane. *Applied Biochemistry and Biotechnology* **2010**, *160*, 156-167.
15. Zhou, H.; Su, Y.; Chen, X.; Wan, Y. Separation of Acetone, Butanol and Ethanol (ABE) from Dilute Aqueous Solutions by Silicalite-1/PDMS Hybrid Pervaporation Membranes. *Separation and Purification Technology* **2011**, *79*, 375-384.
16. Guo, J.; Zhang, G.; Wu, W.; Ji, S.; Qin, Z.; Liu, Z. Dynamically Formed Inner Skin Hollow Fiber polydimethylsiloxane/polysulfone Composite Membrane for Alcohol Permselective Pervaporation. *Chemical Engineering Journal* **2010**, *158*, 558-565.
17. Li, S.; Srivastava, R.; Parnas, R. S. Study of in Situ 1-Butanol Pervaporation from A-B-E Fermentation using a PDMS Composite Membrane: Validity of Solution-Diffusion Model for Pervaporative A-B-E Fermentation. *Biotechnology Progress* **2011**, *27*, 111-120.
18. Li, S.; Srivastava, R.; Parnas, R. S. Separation of 1-Butanol by Pervaporation using a Novel Tri-Layer PDMS Composite Membrane. *Journal of Membrane Science* **2010**, *363*, 287-294.
19. Huang, J.; Meagher, M. M. Pervaporative Recovery of n-Butanol from Aqueous Solutions and ABE Fermentation Broth using Thin-Film Silicalite-Filled Silicone Composite Membranes. *Journal of Membrane Science* **2001**, *192*, 231-242.
20. Fouad, E. A.; Feng, X. Pervaporative Separation of n-Butanol from Dilute Aqueous Solutions using Silicalite-Filled Poly(Dimethyl Siloxane) Membranes. *Journal of Membrane Science* **2009**, *339*, 120-125.
21. Pribic, P.; Roza, M.; Zuber, L. How to Improve the Energy Savings in Distillation and Hybrid Distillation-Pervaporation Systems. *Separation Science and Technology* **2006**, *41*, 2581-2602.
22. Shao, P.; Huang, R. Y. M. Polymeric Membrane Pervaporation. *Journal of Membrane Science* **2007**, *287*, 162-179.
23. Sommer, S.; Klinkhammer, B.; Schleger, M.; Melin, T. Performance Efficiency of Tubular Inorganic Membrane Modules for Pervaporation. *AIChE J.* **2005**, *51*, 162-177.
24. Karlsson, H. O. E.; Traegardh, G. Heat Transfer in Pervaporation. *Journal of Membrane Science* **1996**, *119*, 295-306.
25. Boeddeker, K. W.; Bengtson, G.; Pingel, H.; Dozel, S. Pervaporation of High Boilers using Heated Membranes. *Desalination* **1993**, *90*, 249-257.

26. Ho, W. S. W.; Sirkar, K. K., In *Membrane Handbook*; Van Nostrand Reinhold: New York, 1992; .
27. Storti, B.; Elisei, F.; Abbruzzetti, S.; Viappiani, C.; Latterini, L. One-Pot Synthesis of Gold Nanoshells with High Photon-to-Heat Conversion Efficiency. *Journal of Physical Chemistry, C* **2009**, *113*, 7516-7521.
28. Cortie, M. B.; Xu, X.; Chowdhury, H.; Zareie, H.; Smith, G. Plasmonic Heating of Gold Nanoparticles and its Exploitation. *Proceedings of SPIE* **2005**, *5649*, 565-573.
29. Grua, P.; Morreeuw, J. P.; Bercegol, H.; Jonusauskas, G.; Vallee, F. Electron Kinetics and Emission for Metal Nanoparticles Exposed to Intense Laser Pulses. *Physical Review B* **2003**, *68*, 035424/1-035424/12.
30. Voisin, C.; Del Fatti, N.; Christofilos, D.; Vallee, F. Ultrafast Electron Dynamics and Optical Nonlinearities in Metal Nanoparticles. *Journal of Physical Chemistry, B* **2001**, *105*, 2264-2280.
31. Pissuwan, D.; Valenzuela, S. M.; Cortie, M. B. Therapeutic Possibilities of Plasmonically Heated Gold Nanoparticles. *Trends in Biotechnology* **2006**, *24*, 62-67.
32. Avedisian, C. T.; Cavicchi, R. E.; McEuen, P. L.; Zhou, X. Nanoparticles for Cancer Treatment: Role of Heat Transfer. *Annals of the New York Academy of Sciences* **2009**, *1161*, 62-73.
33. Tong, L.; Zhao, Y.; Huff, T. B.; Hansen, M. N.; Wei, A.; Cheng, J. X. Gold Nanorods Mediate Tumor Cell Death by Compromising Membrane Integrity. *Advanced Materials* **2007**, *19*, 3136.
34. Skirtach, A. G.; Dejugnat, C.; Braun, D.; Sussha, A. S.; Rogach, A. L.; Parak, W. J.; Mohwald, H.; Sukhorukov, G. B. The Role of Metal Nanoparticles in Remote Release of Encapsulated Materials. *Nano Letters* **2005**, *5*, 1371-1377.
35. Seol, Y.; Carpenter, A. E.; Perkins, T. T. Gold Nanoparticles: Enhanced Optical Trapping and Sensitivity Coupled with Significant Heating. *Optics Letters* **2006**, *31*, 2429-2431.
36. Hashimoto, S.; Uwada, T.; Hagiri, M.; Takai, H.; Ueki, T. Gold Nanoparticle-Assisted Laser Surface Modification of Borosilicate Glass Substrates. *Journal of Physical Chemistry, C* **2009**, *113*, 20640-20647.
37. Halabica, A.; Idrobo, J. C.; Pantelides, S. T.; Magruder, R. H.,III; Pennycook, S. J.; Haglund, R. F., Jr Pulsed Infrared Laser Annealing of Gold Nanoparticles Embedded in a Silica Matrix. *Journal of Applied Physics* **2008**, *103*, 083545/1-083545/4.

38. Aguirre, C. M.; Moran, C. E.; Young, J. F.; Halas, N. J. Laser-Induced Reshaping of Metallodielectric Nanoshells Under Femtosecond and Nanosecond Plasmon Resonant Illumination. *Journal of Physical Chemistry, B* **2004**, *108*, 7040-7045.
39. Cao, L.; Barsic, D. N.; Guichard, A. R.; Brongersma, M. L. Plasmon-Assisted Local Temperature Control to Pattern Individual Semiconductor Nanowires and Carbon Nanotubes. *Nano Letters* **2007**, *7*, 3523-3527.
40. Yu, J.; Dai, G.; Huang, B. Fabrication and Characterization of Visible-Light-Driven Plasmonic Photocatalyst Ag/AgCl/TiO₂ Nanotube Arrays. *Journal of Physical Chemistry, C* **2009**, *113*, 16394-16401.
41. Yen, C.; El-Sayed, M. A. Plasmonic Field Effect on the Hexacyanoferrate (III)-Thiosulfate Electron Transfer Catalytic Reaction on Gold Nanoparticles: Electromagnetic Or Thermal?. *Journal of Physical Chemistry, C* **2009**, *113*, 19585-19590.
42. Adleman, J. R.; Boyd, D. A.; Goodwin, D. G.; Psaltis, D. Heterogenous Catalysis Mediated by Plasmon Heating. *Nano Letters* **2009**, *9*, 4417-4423.
43. Jain, P. K.; Lee, K. S.; El-Sayed, I. H.; El-Sayed, M. A. Calculated Absorption and Scattering Properties of Gold Nanoparticles of Different Size, Shape, and Composition: Applications in Biological Imaging and Biomedicine. *Journal of Physical Chemistry, B* **2006**, *110*, 7238-7248.
44. Ahn, W.; Roper, D. K. Transformed Gold Island Film Improves Light-to-Heat Transduction of Nanoparticles on Silica Capillaries. *Journal of Physical Chemistry C* **2008**, *112*, 12214-12218.
45. Russell, A. G.; McKnight, M. D.; Sharp, A. C.; Hestekin, J. A.; Roper, D. K. Gold Nanoparticles Allow Optoplasmonic Evaporation from Open Silica Cells with a Logarithmic Approach to Steady-State Thermal Profiles. *Journal of Physical Chemistry, C* **2010**, *114*, 10132-10139.
46. Seader, J. D.; Henley, E. J. In *Separation Process Principles*; Wiley, John & Sons, Incorporated: Hoboken, NJ, 2006; .
47. Gomez, M. T.; Klein, A.; Repke, J.; Wozny, G. A New Energy-Integrated Pervaporation Distillation Approach. *Desalination* **2008**, *224*, 28-33.
48. Gomez, M. T.; Repke, J.; Kim, D.; Yang, D. R.; Wozny, G. Reduction of Energy Consumption in the Process Industry using a Heat-Integrated Hybrid Distillation Pervaporation Process. *Industrial & Engineering Chemistry Research* **2009**, *48*, 4484-4494.
49. Fernandez, E.; Geerdink, P.; Goetheer, E. L. V. Thermo Pervap: The Next Step in Energy Efficient Pervaporation. *Desalination* **2010**, *250*, 1053-1055.

50. Tsujita, Y.; Yoshimizu, H.; Nakai, Y.; Kinoshita, T. Control of Gas Permeability of Polymeric Membrane by Microwave Irradiation. *Polymeric Materials: Science and Engineering* **2001**, 85, 583.
51. Nakai, Y.; Yoshimizu, H.; Tsujita, Y. Enhanced Gas Permeability of Cellulose Acetate Membranes Under Microwave Irradiation. *Journal of Membrane Science* **2005**, 256, 72-77.
52. Nakai, Y.; Tsujita, Y.; Yoshimizu, H. Control of Gas Permeability for Cellulose Acetate Membrane by Microwave Irradiation. *Desalination* **2002**, 145, 375-377.
53. Wnuk, R.; Chmiel, H. Direct Heating of Composite Membranes in Pervaporation and Gas Separation Processes. *Journal of Membrane Science* **1992**, 68, 293-300.
54. Vanherck, K.; Hermans, S.; Verbiest, T.; Vankelecom, I. Using the Photothermal Effect to Improve Membrane Separations Via Localized Heating. *Journal of Materials Chemistry* **2011**, 21, 6079-6087.
55. Vanherck, K.; Vankelecom, I.; Verbiest, T. Improving Fluxes of Polyimide Membranes Containing Gold Nanoparticles by Photothermal Heating. *Journal of Membrane Science* **2011**, 373, 5-13.
56. Zhang, Q.; Xu, J.; Liu, Y.; Chen, H. In-Situ Synthesis of Poly(Dimethylsiloxane)-Gold Nanoparticles Composite Films and its Application in Microfluidic Systems. *Lab on a Chip* **2008**, 8, 352-357.
57. Russell, A.; Schwarz, S.; Heskekin, J.; Roper, D. K. **2012** (*In Preparation*).
58. Bergstrom, D.; Powell, J.; Kaplan, A. F. K. The Absorptance of Steels to Nd:YLF and Nd:YAG Laser Light at Room Temperature. *Applied Surface Science* **2007**, 253, 5017-5028.
59. Yampolskii, Y.; Pinnau, I.; Freeman, B. D.; (Eds.) In Materials Science of Membranes for Gas and Vapor Separation. **2006**, 445.
60. Wijmans, J. G.; Baker, R. W. The Solution-Diffusion Model: A Review. *Journal of Membrane Science* 1995, 107, 1-21.
61. Feng, X.; Huang, R. Y. M. Liquid Separation by Membrane Pervaporation: A Review. *Industrial & Engineering Chemistry Research* **1997**, 36, 1048-1066.
62. Harris, N.; Ford, M. J.; Cortie, M. B. Optimization of Plasmonic Heating by Gold Nanospheres and Nanoshells. *Journal of Physical Chemistry, B* **2006**, 110, 10701-10707.
63. Volkov, A. N.; Sevilla, C.; Zhigilei, L. V. Numerical Modeling of Short Pulse Laser Interaction with Au Nanoparticle Surrounded by Water. *Applied Surface Science* **2007**, 253, 6394-6399.

64. Hu, M.; Hartland, G. V. Heat Dissipation for Au Particles in Aqueous Solution: Relaxation Time Versus Size. *Journal of Physical Chemistry, B* **2002**, *106*, 7029-7033.
65. Lapotko, D. Optical Excitation and Detection of Vapor Bubbles Around Plasmonic Nanoparticles. *Optics Express* **2009**, *17*, 2538-2556.
66. Kotaidis, V.; Dahmen, C.; von Plessen, G.; Springer, F.; Plech, A. Excitation of Nanoscale Vapor Bubbles at the Surface of Gold Nanoparticles in Water. *Journal of Physical Chemistry* **2006**, *124*, 184702/1-184702/7.
67. Lukianova-Hleb, E. Y.; Lapotko, D. O. Influence of Transient Environmental Photothermal Effects on Optical Scattering by Gold Nanoparticles. *Nano Letters* **2009**, *9*, 2160-2166.
68. Hu, M.; Petrova, H.; Hartland, G. V. Investigation of the Properties of Gold Nanoparticles in Aqueous Solution at Extremely High Lattice Temperatures. *Chemical Physics Letters* **2004**, *391*, 220-225.
69. Lapotko, D. Pulsed Photothermal Heating of the Media during Bubble Generation Around Gold Nanoparticles. *International Journal of Heat and Mass Transfer* **2009**, *52*, 1540-1543.
70. Lapotko, D.; Lukianova, E. Laser-Induced Micro-Bubbles in Cells. *International Journal of Heat and Mass Transfer* **2004**, *48*, 227-234.
71. Richardson, H. H.; Carlson, M. T.; Tandler, P. J.; Hernandez, P.; Govorov, A. O. Experimental and Theoretical Studies of Light-to-Heat Conversion and Collective Heating Effects in Metal Nanoparticle Solutions. *Nano Letters* **2009**, *9*, 1139-1146.
72. Roper, D. K.; Ahn, W.; Hoepfner, M. Microscale Heat Transfer Transduced by Surface Plasmon Resonant Gold Nanoparticles. *Journal of Physical Chemistry, C* **2007**, *111*, 3636.
73. Hoepfner, M. P.; Roper, D. K. Describing Temperature Increases in Plasmon-Resonant Nanoparticle Systems. *Journal of Thermal Analysis and Calorimetry* **2009**, *98*, 197-202.
74. Russell, A. G.; McKnight, M. D.; Hestekin, J. A.; Roper, D. K. Thermodynamics of Optoplasmonic Heating in Fluid-Filled Gold-Nanoparticle-Plated Capillaries. *Langmuir* **2011**, *27*, 7799-7805.
75. Ahn, W.; Taylor, B.; Dall'Asen, A. G.; Roper, D. K. Electroless Gold Island Thin Films: Photoluminescence and Thermal Transformation to Nanoparticle Ensembles. *Langmuir* **2008**, *24*, 4174-4184.
76. Jang, G.; Roper, D. K. Continuous-Flow Electroless Plating Enhances Optical Features of Au Films and Nanoparticles. *Journal of Physical Chemistry, C* **2009**, *113*, 19228-19236.

77. Cengel, Y. A. In *Heat and Mass Transfer: A Practical Approach*; McGraw-Hill: New York, NY, 2007.
78. Smith, J. M.; Van Ness, H. C.; Abbot, M. M. In *Introduction to Chemical Engineering Thermodynamics*; McGraw-Hill: New York, NY, 2005.
79. Link, S.; El-Sayed, M. A. Size and Temperature Dependence of the Plasmon Absorption of Colloidal Gold Nanoparticles. *Journal of Physical Chemistry, B* **1999**, *103*, 4212-4217.
80. Mulder, M.; Editor Basic Principles of Membrane Technology, Second Edition. **1996**, 564.
81. Vankelecom, I. F. J.; Depre, D.; De Beukelaer, S.; Uytterhoeven, J. B. Influence of Zeolites in PDMS Membranes: Pervaporation of Water/Alcohol Mixtures. *Journal of Physical Chemistry* **1995**, *99*, 13193-13197.
82. Deuschle, J. K.; de Souza, E. J.; Arzt, E.; Enders, S. Nanoindentation Studies on Crosslinking and Curing Effects of PDMS. *International Journal of Materials Research* **2010**, *101*, 1014-1023.
83. Stafie, N.; Stamatialis, D. F.; Wessling, M. Effect of PDMS Cross-Linking Degree on the Permeation Performance of PAN/PDMS Composite Nanofiltration Membranes. *Separation and Purification Technology* **2005**, *45*, 220-231.
84. Ci, L.; Suhr, J.; Pushparaj, V.; Zhang, X.; Ajayan, P. M. Continuous Carbon Nanotube Reinforced Composites. *Nano Letters* **2008**, *8*, 2762-2766.
85. Niklaus, M.; Shea, H. R. Electrical Conductivity and Young's Modulus of Flexible Nanocomposites made by Metal-Ion Implantation of Polydimethylsiloxane: The Relationship between Nanostructure and Macroscopic Properties. *Acta Materialia* **2010**, *59*, 830-840.
86. Goyal, A.; Kumar, A.; Patra, P. K.; Mahendra, S.; Tabatabaei, S.; Alvarez, P. J. J.; John, G.; Ajayan, P. M. In Situ Synthesis of Metal Nanoparticle Embedded Free Standing Multifunctional PDMS Films. *Macromolecular Rapid Communications* **2009**, *30*, 1116-1122.
87. Mata, A.; Fleischman, A. J.; Roy, S. Characterization of Polydimethylsiloxane (PDMS) Properties for Biomedical micro/nanosystems. *Biomedical Microdevices* **2005**, *7*, 281-293.
88. Ryu, D.; Loh, K. J.; Ireland, R.; Karimzada, M.; Yaghmaie, F.; Gusman, A. M. In Situ Reduction of Gold Nanoparticles in PDMS Matrices and Applications for Large Strain Sensing. *Smart Structures and Systems* **2011**, *8*, 471-486.
89. Kumar, R.; Pandey, A. K.; Tyagi, A. K.; Dey, G. K.; Ramagiri, S. V.; Bellare, J. R.; Goswami, A. In Situ Formation of Stable Gold Nanoparticles in Polymer Inclusion Membranes. *Journal of Colloid and Interface Science* **2009**, *337*, 523-530.

90. Vanherck, K.; Verbiest, T.; Vankelecom, I. Comparison of Two Synthesis Routes to Obtain Gold Nanoparticles in Polyimide. *Journal of Physical Chemistry, C* **2012**, *116*, 115-125.
91. Haiss, W.; Thanh, N. T. K.; Aveyard, J.; Fernig, D. G. Determination of Size and Concentration of Gold Nanoparticles from UV-Vis Spectra. *Analytical Chemistry* **2007**, *79*, 4215-4221.
92. Liu, X.; Worden, J. G.; Huo, Q.; Brennan, J. P. Kinetic Study of Gold Nanoparticle Growth in Solution by Brust-Schiffrin Reaction. *Journal of Nanoscience and Nanotechnology* **2006**, *6*, 1054-1059.
93. Caseri, W. Nanocomposites of Polymers and Metals or Semiconductors: Historical Background and Optical Properties. *Macromolecular Rapid Communications* **2000**, *21*, 705-722.
94. Liu, X.; Atwater, M.; Wang, J.; Huo, Q. Extinction Coefficient of Gold Nanoparticles with Different Sizes and Different Capping Ligands. *Colloids and Surfaces, B* **2007**, *58*, 3-7.
95. Jana, N. R.; Gearheart, L.; Murphy, C. J. Evidence for Seed-Mediated Nucleation in the Chemical Reduction of Gold Salts to Gold Nanoparticles. *Chemistry of Materials* **2001**, *13*, 2313-2322.
96. Murillo, L. E.; Viera, O.; Vicuña, E.; Briano, J. G.; Castro, M. E.; Ishikawa, Y.; Irizarry, R.; Solá, L. In *In Growth Kinetics of Gold Nanoparticles*; Technical Proceedings of the 2002 International Conference on Computational Nanoscience and Nanotechnology; 2002; pp 435-438.
97. Caseri, W. R. Nanocomposites of Polymers and Inorganic Particles: Preparation, Structure and Properties. *Material Science and Technology* **2006**, *22*, 807-817.
98. Nussbaumer, R. J. Phd Thesis No. 15516, ETH Zurich, 2004.
99. Berry, K.; Russell, A.; Blake, P.; Roper, D. K. Gold Nanoparticles Reduced in situ and Dispersed in Polymer Thin Films: Optical and Thermal Properties. **2012**, *Nanotechnology (In Revision)*.
100. Berry, K.; Russell, A.; Roper, D. K. **2012**, *(In Preparation)*.